IEEE Access
Multidisciplinary | Rapid Review | Open Access Journal

Received 22 February 2024, accepted 25 March 2024, date of publication 28 March 2024, date of current version 4 April 2024.

Digital Object Identifier 10.1109/ACCESS.2024.3382719

RESEARCH ARTICLE

Performance Analysis of In-Band-Full-Duplex Multi-Cell Wideband IAB Networks

JUNKAI ZHANG[1,2], (Member, IEEE), AND THARMALINGAM RATNARAJAH[2], (Senior Member, IEEE)
[1]School of Mathematics and Statistics, Xi'an Jiaotong University, Xi'an 710049, China
[2]Institute for Imaging, Data and Communications (IDCOM), The University of Edinburgh, EH9 3BF Edinburgh, U.K.

Corresponding author: Junkai Zhang (jk.zhang@xjtu.edu.cn)

This work was supported by U.K. Engineering and Physical Sciences Research Council (EPSRC) under Grant EP/T021063/1.

ABSTRACT This study analyzes the performance of 3rd Generation Partnership Project (3GPP)-inspired multi-cell wideband single-hop backhaul millimeter-wave-in-band-full-duplex (IBFD)-integrated access and backhaul (IAB) networks using stochastic geometry. We modeled the wired-connected Next Generation NodeBs (gNBs) as the Matérn hard-core point process (MHCPP) to meet real-world deployment requirements and reduce the cost caused by wired connections in the network. We first derive association probabilities that reflect the likelihood that typical user-equipment is served by a gNB or an IAB-node based on the maximum long-term averaged biased-received-desired-signal power criteria. Furthermore, by leveraging the composite Gamma-Lognormal distribution, we derived the closed-form signal to interference plus noise ratio coverage, capacity with outage, and ergodic capacity of the network. To avoid underestimating the noise, we consider the sidelobe gain on the inter-cell interference links and analog-to-digital converter quantization noise. Compared with half-duplex transmission, the numerical results show an enhanced capacity with outage and ergodic capacity provided by the IBFD under successful self-interference cancellation. We also study how the power bias and density ratio of the IAB-node to gNB and the hard-core distance can affect system performance.

INDEX TERMS Millimeter-wave, integrated access and backhaul, in-band-full-duplex, Matérn hard-core point process, stochastic geometry.

I. INTRODUCTION

Millimeter-wave (mmWave) communications have been provided to satisfy the urgent demand for large available bandwidth in beyond fifth-generation (B5G) communications, as the number of wireless devices increases sharply in current networks [2], [3]. Although a large available bandwidth of 30-300 GHz can significantly increase the capacity of the wireless network, the path loss becomes more severe than that in microwave communications because the effective antenna aperture is proportional to the wavelength. Therefore, dense base station (BS) deployment with large-scale antenna arrays is required. For hardware and power efficiency, fully-connected/subarray hybrid beamforming is used for mmWave communication [4], [5].

To further explore the benefits of the mmWave spectrum, in-band-full-duplex (IBFD) transmission, where transmission and reception occur at the same time and frequency band, has been proposed [6], [7]. Compared with half-duplex (HD) transmission, the IBFD scheme provides twice the spectral efficiency (SE) and half the latency [8]. However, dealing with self-interference (SI), which can be more than 100 dB higher than the desired signal, is the biggest challenge in realizing IBFD transmission. Fortunately, a combination of antenna [9], analog [8], [10], and digital [11] SI cancellation (SIC) can achieve satisfactory performance in mmWave IBFD networks.

Moreover, integrated access and backhaul (IAB) networks have been studied in the technical specifications–TR 38.874 (Rel. 16) provided by the 3rd Generation Partnership Project (3GPP) [12], where wireless backhaul is introduced instead of fiber connections. Plug-and-play deployment [12], multi-hop networks [13], and performance analysis [14] of IAB

The associate editor coordinating the review of this manuscript and approving it for publication was Adao Silva.

networks have been used in recent research. Although the authors in [15] concluded that all-wired networks (i.e., all BSs connected to the core network by fiber directly) provide better performance than IAB networks, IAB networks provide a good solution for reducing the deployment cost in mmWave communications. Although we designed single-cell wideband single-hop backhaul mmWave-IBFD-IAB networks in [2], [11], more profound studies on the performance analysis of multi-cell wideband single-hop backhaul mmWave-IBFD-IAB networks are lacking in the literature, which is the main subject of this work.

In previous studies [3], [14], [16], [17], the performance of IAB networks was evaluated. However, none of these studies considered IBFD transmission and hybrid beamforming, except for [3]. In addition, in terms of the distribution of small fading, only [14] considered the Nakagami-M distribution, which is more suitable for mmWave communications than the Rayleigh distribution because the Rayleigh fading model for sub-6 GHz communications is predicated on a large amount of local scattering, which is not the case for mmWave communications [18].

Meanwhile, stochastic geometry is a powerful tool for analyzing the performance of wireless networks such as mmWave cellular networks [19], heterogeneous cellular networks [20], and unmanned aerial vehicle (UAV) networks [21]. However, to the best of our knowledge, work on IAB systems with stochastic geometry is insufficient. For instance, the performance of mmWave-HD-IAB systems was analyzed in [16] with two resource allocation strategies at Next Generation NodeBs (gNBs), i.e., integrated resource allocation and orthogonal resource allocation. The authors in [3] studied the performance of mmWave-IBFD-IAB systems in wireless edge caching. Bandwidth partitioning for mmWave-HD-IAB systems with performance analysis by stochastic geometry was studied in [14]. A multi-cell model of a single-tier mmWave-HD-IAB system was proposed in [17]. However, in the aforementioned stochastic geometry-related IAB networks studies, only the work in [17] considered the shadowing effect in mmWave communications. Therefore, to analyze a more general mmWave-IAB network suitable for beyond 5G communications, we consider IBFD, hybrid beamforming, Nakagami-M small fading, and lognormal shadowing effects in this work.

In the real world, BSs are not entirely deployed randomly or regularly, which results in the deterministic or Poisson point process (PPP) model becoming insufficient. Therefore, non-Poisson models are preferred for modeling real-world BS deployment. For analytical tractability, the authors of [22] suggested a method that uses PPP to approximate the signal-to-interference-ratio meta-distribution for non-Poisson networks, which can provide good accuracy. In this work, to model the deployment of wired-connected gNBs, that is, IAB donors, the Matérn hard-core point process (MHCPP) was applied, where a hard-core distance (i.e., the minimum distance between two gNBs separated in the network) was utilized. The MHCPP model reflects the repulsion between gNBs because gNBs act as wired-anchored BSs. Two gNBs should not be too close or overlapping. Moreover, while providing satisfactory service quality, MHCPP generates a lower density of gNBs than PPP, which avoids the high cost of wired connections. Although MHCPP has been applied to the modeling of UAVs [23], multi-cell IBFD cellular networks [24], and cloud radio access networks [25], to the best of our knowledge, this is the first study to introduce MHCPP into the analysis of multi-cell mmWave-IBFD-IAB networks.

In this study, we evaluate the performance of multi-cell wideband single-hop backhaul mmWave-IBFD-IAB networks using stochastic geometry. The main contributions of this study are summarized as follows. A comparison between the existing stochastic geometry-based studies and our work is summarized in Table. 1.

- Unlike previous studies on mmWave communications using stochastic geometry, which do not consider hybrid beamforming, we analyze the performance with energy-efficient subarray-based hybrid beamforming because mmWave communications need to adopt large-scale antenna arrays. Hybrid beamforming has lower hardware cost and power consumption than transitional full digital beamforming because the number of RF chains required is reduced.
- Unlike prior studies on IAB networks, which use PPP to model the location of gNBs, we use MHCPP to meet the real-world deployment scenario in which BSs are deployed in the non-Poisson model. In this manner, wired-connected gNBs, which act as anchored BSs, can be deployed without overlapping or being too close. In addition, MHCPP produces fewer gNBs than PPP, which reduces the cost of deploying wired gNBs. We use the probability generating functional (PGFL) of PPP to estimate the mean interference from gNBs in the backhaul link and gNB-associated access link, which makes the analysis more tractable.
- Instead of analyzing the performance of mmWave-HD-all-wired networks, we consider mmWave-IBFD-IAB networks, which satisfy the requirement of enhanced communication performance and dense deployment with less cost in beyond 5G communications. The IAB-nodes operate in the IBFD mode for simultaneous transmission and reception. Assuming successful SIC, only the residual SI (RSI), modeled as Gaussian noise, is considered, whose power is modeled as a fraction of the transmit power [3], [11], [26].
- To accurately model the channel and path loss for mmWave communications, we consider Nakagami-M small fading and include the lognormal shadowing effect in the path loss model, which is different from most of the existing literature on mmWave communications using stochastic geometry. For tractability, we introduced the closed-form statistical property of the composite Gamma-Lognormal (GL) distribution to derive the analytical results.

TABLE 1. Comparison between existing stochastic geometry-based studies and our work.

	mmWave	IBFD	IAB	Hybrid Beamforming	Nakagami-M	Lognormal	MHCPP	Sidelobe Gain	Quantization Noise
[3]	√	√	√	√				√	
[5]	√			√		√		√	
[14]	√		√		√				
[16]	√		√						
[17]	√		√			√			
[19]	√				√				
[21]	√				√		√		
[24]		√					√		
[26]		√	√						
[27]	√				√			√	
[28]	√			√		√		√	
[29]					√	√			
Our work	√	√	√	√	√	√	√	√	√

- To avoid underestimation of noise and interference, we consider the sidelobe gain for the inter-cell interference links and analog-to-digital converter (ADC) quantization noise.

Numerical results show that by tuning the bias ratio of the IAB-node to gNB, signal-to-interference-plus-noise-ratio (SINR) coverage yields a convex-like curve at a fixed SINR threshold. With a selected bias ratio (e.g., 0 dB), the capacity with outage of the IBFD scheme outperforms that of the HD scheme, regardless of the RSI power. In addition, for our default simulation setting, at SINR $=$ 0 dB, the ADC quantization noise effect becomes negligible at a resolution of approximately five bits, which emphasizes the feasibility of using a low resolution ADC in our proposed network. Moreover, under the same gNB density, the network ergodic capacity obtained by deploying gNBs with the PPP-based model is less than that obtained by deploying gNBs with the MHCPP-based model; the larger the hard-core distance, the higher the ergodic capacity. In addition, with successful SIC, the ergodic capacity increases as the density ratio of the IAB-node to the gNB increases.

The rest of this paper is organized as follow. Section II introduces system model including IAB network architecture, spatial arrangement, and propagation model. Followed by Section III provides antenna configuration and beamforming design. Then, the SINR characterization is formulated in Section IV, which is used for deriving the analytical equations of the performance metrics in Section V. Finally, we show numerical results in Section VI and draw a brief conclusion in Section VII.

Notations: $\mathcal{B}, \mathbf{B}, \mathbf{b}$, b represent the set, the matrix, the vector, and the scalar, respectively. $\mathbf{B}^H$, $\mathbf{B}^{-1}$, and $\mathbf{B}^T$ are the Hermitian, inverse, and transpose of $\mathbf{B}$, respectively. blkdiag $[\mathbf{B}_1, \mathbf{B}_2]$ is the block diagonal matrix formed by matrices $\mathbf{B}_1$ and $\mathbf{B}_2$. $\|\cdot\|_F$ denotes the Frobenius norm. $|b|$ is the norm of b. $||\mathbf{b}||$ is the norm of $\mathbf{b}$. C_n^k is the possible combinations of k elements out of a group of n elements where order does not matter. $\mathcal{N}(m, n)$ represents a normal distribution with mean m and variance n. $\ln\mathcal{N}(m, n)$ denotes a lognormal distribution with parameters m and n. $\mathcal{U}[a, b]$ represents a uniform distribution between a and b.

II. SYSTEM MODEL

A. IAB NETWORK TOPOLOGY

We consider the downlink of a standalone single-hop backhaul IAB network with a spanning tree (ST) topology consisting of the following nodes:

- IAB donor: This is also called a gNB, which is a single logical node. The gNB connects to the next-generation core network using fibers and wirelessly transmits signals to other types of nodes in the network.
- IAB-node: This node operates in the IBFD manner, contributes SI from its transmitter to its receiver, and uses wireless links to communicate with others. Owing to the single-hop backhaul and ST topology, an IAB-node has only one parent gNB for backhauling.
- User-equipment (UE): It receives the desired signal from its serving gNB or IAB-node.

The backhaul link is the wireless link between the gNB and the IAB-node, whereas the access link is that between the UE and the gNB or the IAB-node. More details of the 3GPP architecture can be found in our recent study [2]. An illustration of the proposed model is shown in Fig. 1(a). In this study, the gNBs and IAB-nodes formed two different tiers. Multi-hop backhaul IAB networks will not be considered because of the challenge of network configuration, and the feasibility of using stochastic geometry in this scenario [16].

B. SPATIAL ARRANGEMENT

There are two types of MHCPP: both are generated by thinning the parent PPP. In Type I, a point and its neighbors whose distance is less than the hard-core distance are removed from the parent PPP. In type II, each point is assigned a random number between 0 and 1 as their marks; only points that have larger marks and are within the hard-core region of their neighbors are removed [30]. In this study, we utilize MHCPP Type II[1] to capture the location of gNBs. Consider that gNBs are distributed according to an MHCPP Φ_{m} with density λ_{m} and hard-core distance ξ on $\mathbb{R}^2$, where the density is defined by the dependent thinning of a parent homogeneous PPP $\widetilde{\Phi}_{\mathrm{m}}$

[1]Under the same parent PPP density, the thinning rule of MHCPP type II is more relaxed than that of MHCPP Type I, which can provide a higher density of gNB to satisfy the dense deployment condition for mmWave communications.

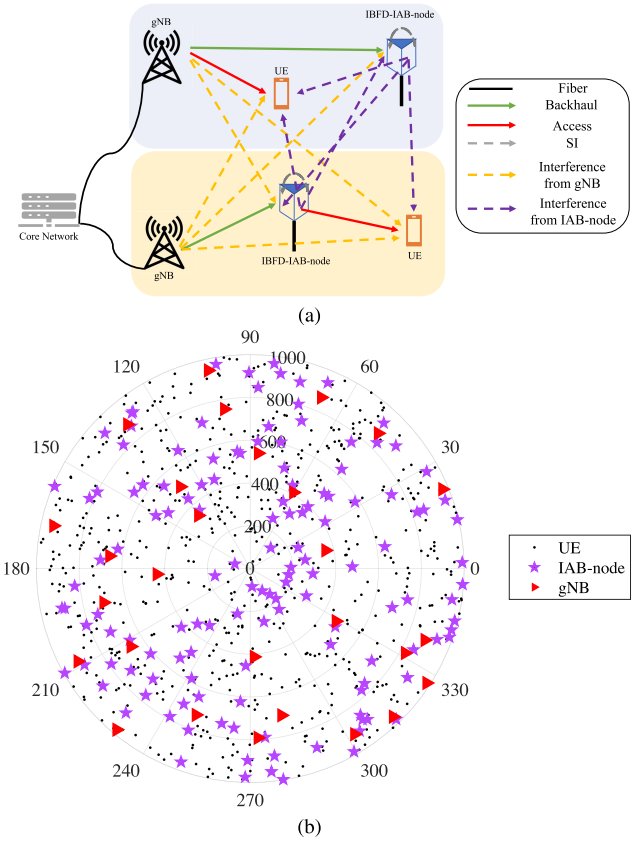

FIGURE 1. (a) Illustration of a multi-cell single-hop backhaul mmWave-IBFD-IAB network. (b) A realized mmWave-IBFD-IAB network. $R_0 = 1000$m, $\lambda_m = 1 \times 10^{-5}/\text{m}^2$, $\lambda_s = 4 \times 10^{-5}/\text{m}^2$, $\lambda_u = 2 \times 10^{-4}/\text{m}^2$, $\xi = 100$m.

with density of $\widetilde{\lambda}_m$. Given that the probability of an arbitrary point in the parent PPP is retained for MHCPP Type II as

$$\rho = \frac{1 - e^{-\pi \xi^2 \widetilde{\lambda}_m}}{\pi \xi^2 \widetilde{\lambda}_m}, \tag{1}$$

where $\lambda_m = \rho \widetilde{\lambda}_m$ [31]. The IAB-nodes and UE are drawn from two independent homogeneous PPP Φ_s and Φ_u with densities λ_s and λ_u on $\mathbb{R}^2$, respectively. Our analysis was performed on a circular region with a radius R_0. A realization of such a network is illustrated in Fig. 1(b).

C. PROPAGATION MODEL

1) BLOCKAGE MODEL

At mmWave frequencies, the signals are easily blocked by obstacles in the propagation environment, which results in the coexistence of line-of-sight (LoS) and non-line-of-sight (NLoS) propagations. Blockages typically form a process of random shapes, for example, a Boolean scheme of rectangles [32]. In this section, the probability of being LoS $p_L(r)$ or NLoS $p_N(r)$ transmission is modeled by a two-state exponential blockage model with respect to the blockage density constant ϵ and the link distance r [27], which is expressed as

$$\begin{cases} p_L(r) = e^{-\epsilon r}, \\ p_N(r) = 1 - e^{-\epsilon r}. \end{cases} \tag{2}$$

Note that we adopt the above model for IAB-nodes because gNBs can be located well above ground level because of the role of anchored BSs and are usually placed on open ground with fewer obstacles to increase the likelihood of LoS links. For tractability, we assume LoS transmission only for the gNB to ease the lack of transformation properties of MHCPP, such as the PGFL. Moreover, we consider the independent blockage effects between the links in this study.

Given the blockage model, we can treat the PPP IAB-nodes Φ_s as the superposition of PPP LoS IAB-nodes $\Phi_{s,L}$ and PPP NLoS IAB-nodes $\Phi_{s,N}$ with densities $\lambda_{s,L}(r) = \lambda_s p_L(r)$ and $\lambda_{s,N}(r) = \lambda_s p_N(r)$, respectively.

2) PATH LOSS MODEL

The path loss model utilized in [17] is adopted in this study to measure the path loss between two nodes located at $\mathbf{x}$ and $\mathbf{y}$. The gain for a single antenna element is given by

$$L(\mathbf{x}, \mathbf{y})[\text{dB}] = \beta + 10\alpha \log_{10} R_{\mathbf{xy}} + \chi, \tag{3}$$

where $\beta = 20 \log_{10}\left(\frac{4\pi f_c}{c}\right)$. f_c, c, α, and $\chi \sim \mathcal{N}(0, \zeta^2)$ denote the carrier frequency, light speed, path loss exponent, and shadowing effect random variable, respectively. $R_{\mathbf{xy}}$ represents the Euclidean distance between $\mathbf{x}$ and $\mathbf{y}$. Therefore, we have $L(\mathbf{x}, \mathbf{y}) = \frac{R_{\mathbf{xy}}^{\alpha}}{10^{-0.1(\beta+\chi)}}$, where $10^{-0.1(\beta+\chi)} \sim \ln\mathcal{N}\left(-0.1\beta \ln 10, (0.1\zeta \ln 10)^2\right)$ is a lognormal distributed random variable.[2] Note that the path loss exponent and Gaussian distributed shadowing effect random variable for the transmissions from gNB are denoted as α_m and $\chi_m \sim \mathcal{N}(0, \zeta_m^2)$, respectively. For the IAB-node, we have the path loss exponent $\alpha_{s,i}$ and shadowing effect random variables $\chi_{s,i} \sim \mathcal{N}(0, \zeta_{s,i}^2)$, where $i = L$ for the LoS IAB-node and $i = N$ for the NLoS IAB-node.

3) CHANNEL MODEL

Assume an OFDM single-path (i.e., flat fading) channel for all blockage scenarios, which leverages the sparsity of the FR2 band channel. A multi-path case will be left in the future. At subcarrier $k = 1, 2, \ldots, K$, the wideband mmWave channel from the node at $\mathbf{x}$ with N_T transmit antennas to the node at $\mathbf{y}$ with N_R receive antennas is given as [4].

$$\mathbf{H}_{\mathbf{yx}}[k] = \sqrt{\frac{N_T N_R}{L(\mathbf{x},\mathbf{y})}} h^{\mathbf{yx}} \gamma[k] \mathbf{a}_R(\bar{\theta}_R^{\mathbf{yx}}, \bar{\phi}_R^{\mathbf{yx}}) \mathbf{a}_T^H(\bar{\theta}_T^{\mathbf{yx}}, \bar{\phi}_T^{\mathbf{yx}}), \tag{4}$$

where $h^{\mathbf{yx}}$ is the small fading gain with a Nakagami-M distribution [33], [34]. $M \in \{M_m, M_{s,L}, M_{s,N}\} \in \mathbb{N}^+$ are Nakagami parameters for the gNB, LoS IAB-node, and NLoS IAB-node, respectively. $\gamma[k] = \sum_{d=0}^{D-1} p(d - \widetilde{\tau}) e^{-j\frac{2\pi kd}{K}}$ with $p(\cdot)$ being the raised-cosine pulse-shaping filter, $\widetilde{\tau} \sim \mathcal{U}[0, D]$ being the normalized path delay, and D denoting the number of delay taps.

[2] If Z is a normally distributed random variable with zero mean and variance σ^2, then $X = e^{m+nZ}$ is a lognormal random variable with parameters $\hat{\mu} = m$ and $\hat{\sigma} = n\sigma$, denoted as $X \sim \ln\mathcal{N}(\hat{\mu}, \hat{\sigma}^2)$ with $\mathbb{E}\{X\} = e^{\hat{\mu}+0.5\hat{\sigma}^2}$.

For simplicity, we leverage the virtual transmit and receive steering vectors $\mathbf{a}_{\mathrm{T}}(\bar{\theta}_{\mathrm{T}}^{\mathbf{yx}}, \bar{\phi}_{\mathrm{T}}^{\mathbf{yx}})$ and $\mathbf{a}_{\mathrm{R}}(\bar{\theta}_{\mathrm{R}}^{\mathbf{yx}}, \bar{\phi}_{\mathrm{R}}^{\mathbf{yx}})$ for the uniform planar array (UPA), respectively, where the azimuth $\bar{\theta}_{\mathrm{T}}^{\mathbf{yx}}/\bar{\theta}_{\mathrm{R}}^{\mathbf{yx}}$ and elevation $\bar{\phi}_{\mathrm{T}}^{\mathbf{yx}}/\bar{\phi}_{\mathrm{R}}^{\mathbf{yx}}$ virtual angles correspond to the angle of departure/arrival (AoD/AoA) [35]. With half-wavelength spaced elements, we have the relationship between the virtual and physical azimuth (elevation) AoD/AoA as $\bar{\theta} = \pi \cos\theta \cos\phi$ ($\bar{\phi} = \pi \sin\theta \cos\phi$), where $\theta \sim \mathcal{U}[0, \pi]$ and $\phi \sim \mathcal{U}[-\frac{\pi}{2}, \frac{\pi}{2}]$ are the physical azimuth and elevation AoD/AoA, respectively. By extending the model in [35], we quantize the virtual azimuth and elevation AoD/AoA to set $\bar{\theta} \in \left\{-\pi, -\pi + \frac{2\pi}{N_{\mathrm{x}}}, \ldots, -\pi + \frac{2\pi(N_{\mathrm{x}}-1)}{N_{\mathrm{x}}}\right\}$ and $\bar{\phi} \in \left\{0, \frac{\pi}{N_{\mathrm{y}}}, \ldots, \frac{\pi(N_{\mathrm{y}}-1)}{N_{\mathrm{y}}}\right\}$ with N_{x} and N_{y} being the number of antennas along x- and y-axis of the UPA. Moreover, we assume that virtual angles are uniformly distributed in their quantized sets for tractability [28]. From the orthogonality of the virtual steering vector, we have $\mathbf{a}^H(\bar{\theta}_1, \bar{\phi}_1)\mathbf{a}(\bar{\theta}_2, \bar{\phi}_2) = 1$ for $\bar{\theta}_1 = \bar{\theta}_2, \bar{\phi}_1 = \bar{\phi}_2$ and 0 otherwise [36, Corollary 2], which gives us an ON/OFF model. Using this ON/OFF model, SINR expressions can be simplified.

Because this work aims to evaluate the performance of IBFD-IAB networks after the SI has been successfully suppressed, only the residual SI, treated as Gaussian noise, whose power is modeled as a fraction of the transmit power, will be considered. Readers are directed to [11] for a hypothetical Rician-like SI channel model and staged SIC strategy.

III. ANTENNA CONFIGURATION AND BEAMFORMING DESIGN

A. ANTENNA CONFIGURATION

The gNB and IAB-node transmitters are adopted with subarray-based hybrid beamforming (i.e., one RF chain connects with only a portion of the antennas), as proposed in [11] and [4]. The gNB has N_{m} subarrays, each having $\frac{N_{\mathrm{T}}^{\mathrm{m}}}{N_{\mathrm{m}}}$ transmit antennas and one RF chain sending a single data stream to serve one UE or IAB-node. Similarly, the IAB-node is equipped with N_{s} subarrays, each with $\frac{N_{\mathrm{T}}^{\mathrm{s}}}{N_{\mathrm{s}}}$ transmitting antennas and a single RF chain sending one data stream to serve an UE. The IAB-node receiver is equipped with $N_{\mathrm{R}}^{\mathrm{s}}$ receiving antennas adopting analog combining to receive information from its serving gNB. The UE receiver has $N_{\mathrm{R}}^{\mathrm{u}}$ antennas with analog combining for communicating with its serving BS.

B. BEAMFORMING DESIGN

According to the subarray hybrid beamforming structure given in [4], the RF and BB precoders at the gNBs and IAB-nodes have the form of $\mathbf{F}_{\mathrm{RF}}^{(\cdot)} = \mathrm{blkdiag}\left[\mathbf{f}_{\mathrm{RF},1}^{(\cdot)}, \mathbf{f}_{\mathrm{RF},2}^{(\cdot)}, \ldots, \mathbf{f}_{\mathrm{RF},N_i}^{(\cdot)}\right] \in \mathbb{C}^{N_{\mathrm{T}}^i \times N_i}$ and $\mathbf{F}_{\mathrm{BB}}^{(\cdot)}[k] = \left[\mathbf{f}_{\mathrm{BB},1}^{(\cdot)}[k], \mathbf{f}_{\mathrm{BB},2}^{(\cdot)}[k], \ldots, \mathbf{f}_{\mathrm{BB},N_i}^{(\cdot)}[k]\right] \in \mathbb{C}^{N_i \times N_i}$, respectively, where $(\cdot)$ is the location of the gNB or IAB-node; $i = \mathrm{m}$ represents the precoders at the gNB and $i = \mathrm{s}$ are those at the IAB-node. The RF combiner at the IAB-node and UE are in the form of $\mathbf{w}_{\mathrm{RF}}^{(\cdot)} \in \mathbb{C}^{N_{\mathrm{R}}^i \times 1}$, where $i = \mathrm{s}$ denotes the combiner at the IAB-node and $i = \mathrm{u}$ is that at the UE.

RF beamformers are realized using phase shifters (PSs) with unit norm entries. According to [28], the optimal RF precoder/combiner that maximizes the desired signal power is to steer the beam in the direction of the AoD/AoA of the desired signal channel. Given the channel from the transmitter at $\mathbf{x}$ to the receiver at $\mathbf{y}$ in (4), owing to the use of subarray-based hybrid beamforming, a subset of the virtual transmit steering vector is used to design the vth column of the RF precoder matrix $\mathbf{F}_{\mathrm{RF}}^{\mathbf{x}}$, that is,

$$\mathbf{f}_{\mathrm{RF},v}^{\mathbf{x}} = \sqrt{N_{\mathrm{T}}^i}\left[\mathbf{a}_{\mathrm{T}}(\bar{\theta}_{\mathrm{T}}^{\mathbf{yx}}, \bar{\phi}_{\mathrm{T}}^{\mathbf{yx}})\right]_{(v-1)\frac{N_{\mathrm{T}}^i}{N_i}+\left(1:\frac{N_{\mathrm{T}}^i}{N_i}\right),:}, \tag{5}$$

where $i = \mathrm{m}$ represents the RF precoder at the gNB, and $i = \mathrm{s}$ denotes that at the IAB-node.

Similarly, the RF combiner is given by the virtual receiver steering vector, that is,

$$\mathbf{w}_{\mathrm{RF}}^{\mathbf{y}} = \sqrt{N_{\mathrm{R}}^i}\mathbf{a}_{\mathrm{R}}(\bar{\theta}_{\mathrm{R}}^{\mathbf{yx}}, \bar{\phi}_{\mathrm{R}}^{\mathbf{yx}}), \tag{6}$$

where $i = \mathrm{s}$ denotes the combiner at the IAB-node, and $i = \mathrm{u}$ denotes that at the UE.

To mitigate the intra-cell interference, the zero-forcing (ZF) BB precoder is utilized at both the gNB and IAB-node. For a transmitter at $\mathbf{x}$, given all its serving receivers at $\mathbf{y}_1, \mathbf{y}_2, \ldots, \mathbf{y}_{N_i}$ (for $i = \mathrm{m}$ if $\mathbf{x}$ is a gNB and $i = \mathrm{s}$ if $\mathbf{x}$ is an IAB-node), the ZF BB precoder matrix can be given as

$$\mathbf{F}_{\mathrm{BB}}^{\mathbf{x}}[k] = \widetilde{\mathbf{H}}_{\mathbf{yx}}^H[k]\left(\widetilde{\mathbf{H}}_{\mathbf{yx}}[k]\widetilde{\mathbf{H}}_{\mathbf{yx}}^H[k]\right)^{-1}, \tag{7}$$

where $\widetilde{\mathbf{H}}_{\mathbf{yx}}[k] = \left(\mathbf{W}_{\mathrm{RF}}^{\mathbf{y}}\right)^H \hat{\mathbf{H}}_{\mathbf{yx}}[k]\mathbf{F}_{\mathrm{RF}}^{\mathbf{x}}$ with $\mathbf{W}_{\mathrm{RF}}^{\mathbf{y}} = \mathrm{blkdiag}[\mathbf{w}_{\mathrm{RF}}^{\mathbf{y}_1}, \mathbf{w}_{\mathrm{RF}}^{\mathbf{y}_2}, \ldots, \mathbf{w}_{\mathrm{RF}}^{\mathbf{y}_{N_i}}]$ and $\hat{\mathbf{H}}_{\mathbf{yx}}[k] = [\mathbf{H}_{\mathbf{y}_1\mathbf{x}}^T[k], \mathbf{H}_{\mathbf{y}_2\mathbf{x}}^T[k], \ldots, \mathbf{H}_{\mathbf{y}_{N_i}\mathbf{x}}^T[k]]^T$.

IV. SINR CHARACTERIZATION

In this section, we derive SINR expressions for the kth subcarrier. According to Slivnyak's theorem [30], given that both IAB-nodes and UEs are homogeneous PPP, we consider typical backhaul and access links without loss of generalization, that is, we derive the typical backhaul (access) link SINR by assuming that the typical IAB-node (UE) is located at the origin $\hat{\mathbf{0}}$ ($\mathbf{0}$). Note that $\mathbf{0}$ and $\hat{\mathbf{0}}$ represent the origins of the same coordinate system.

Assume that we know the channel state information perfectly for all channels, and that all signals are uncorrelated. Let the average total transmit power at the gNB (IAB-node) across all subcarriers be P_{m} (P_{s}). With equal power allocation, each data stream at subcarrier k transmitted from the gNB (IAB-node) has the power of $\frac{P_{\mathrm{m}}}{KN_{\mathrm{m}}}$ $\left(\frac{P_{\mathrm{s}}}{KN_{\mathrm{s}}}\right)$. Moreover, as the ZF precoder is applied, the intra-cell interference can be canceled out; thus, is ignored in the following equations. In addition, the following assumption was made simplify the analysis.

Assumption 1: The channel model in Eq. (4) is a function of k, where k appears only in $\gamma[k]$. Because our work is based

on a probabilistic perspective, for tractability, we assume the normalized path delay to be $\widetilde{\tau} = \frac{D}{2}$, which is the mean of the random variable $\widetilde{\tau}$. Given that the channel is flat fading, all subcarriers experience the same channel conditions. Thus, we have $\mathbb{E}\{|\gamma[k]|^2\} = 1 \forall k$, which makes the channel independent of k [3].

1) BACKHAUL LINK

Assuming that the gNB at $\mathbf{x}_\mathrm{m}$ uses its vth subarray to provide backhaul communication with the typical IAB-node at $\hat{\mathbf{0}}$, the SINR of the typical backhaul link at the kth subcarrier is written as

$$\mathrm{SINR}_{\hat{\mathbf{0}}\mathbf{x}_\mathrm{m}}[k] = \frac{G_\mathrm{b}[k]}{I_{\mathrm{m,b}}[k]+I_{\mathrm{s,b}}[k]+\underbrace{\frac{\eta P_\mathrm{s}}{K}}_{\mathrm{RSI}}+\mathbb{E}\left\{\left|\left(\mathbf{w}_{\mathrm{RF}}^{\hat{\mathbf{0}}}\right)^H \mathbf{n}_\mathrm{b}[k]\right|^2\right\}+\mathbb{E}\{|e_\mathrm{b}[k]|^2\}}, \tag{8a}$$

$$G_\mathrm{b}[k] = \frac{P_\mathrm{m}}{KN_\mathrm{m}}\left|\left(\mathbf{w}_{\mathrm{RF}}^{\hat{\mathbf{0}}}\right)^H \mathbf{H}_{\hat{\mathbf{0}}\mathbf{x}_\mathrm{m}}[k]\mathbf{F}_{\mathrm{RF}}^{\mathbf{x}_\mathrm{m}}\mathbf{f}_{\mathrm{BB},v}^{\mathbf{x}_\mathrm{m}}[k]\right|^2 \approx \frac{P_\mathrm{m}N_\mathrm{T}^\mathrm{m}\left(N_\mathrm{R}^\mathrm{s}\right)^2\widetilde{h}^{\hat{\mathbf{0}}\mathbf{x}_\mathrm{m}}p_{\mathrm{ZF}}(N_\mathrm{T}^\mathrm{m},N_\mathrm{m})}{KN_\mathrm{m}^2R_{\mathbf{x}_\mathrm{m}\hat{\mathbf{0}}}^{\alpha_\mathrm{m}}}, \tag{8b}$$

$$I_{\mathrm{m,b}}[k] = \frac{P_\mathrm{m}}{KN_\mathrm{m}}\left\|\sum_{\substack{\omega\in\\ \Phi_\mathrm{m}\setminus\mathbf{x}_\mathrm{m}}}\left(\mathbf{w}_{\mathrm{RF}}^{\hat{\mathbf{0}}}\right)^H \mathbf{H}_{\hat{\mathbf{0}}\omega}[k]\mathbf{F}_{\mathrm{RF}}^{\omega}\mathbf{F}_{\mathrm{BB}}^{\omega}[k]\right\|^2 \approx \sum_{\substack{\omega\in\\ \Phi_\mathrm{m}\setminus\mathbf{x}_\mathrm{m}}}\frac{P_\mathrm{m}N_\mathrm{T}^\mathrm{m}\left(N_\mathrm{R}^s\right)^2\widetilde{h}^{\hat{\mathbf{0}}\omega}p_{\mathrm{BF}}(N_\mathrm{T}^\mathrm{m},N_\mathrm{R}^\mathrm{s},N_\mathrm{m})}{KN_\mathrm{m}R_{\omega\hat{\mathbf{0}}}^{\alpha_\mathrm{m}}}, \tag{8c}$$

$$I_{\mathrm{s,b}}[k] = \sum_{i\in\{\mathrm{L,N}\}} I_{\mathrm{s,b}}^i[k] = \frac{P_\mathrm{s}}{KN_\mathrm{s}}\left\|\sum_{i\in\{\mathrm{L,N}\}}\sum_{\hat{\omega}\in\Phi_{\mathrm{s},i}\setminus\hat{\mathbf{0}}}\left(\mathbf{w}_{\mathrm{RF}}^{\hat{\mathbf{0}}}\right)^H \mathbf{H}_{\hat{\mathbf{0}}\hat{\omega}}[k]\mathbf{F}_{\mathrm{RF}}^{\hat{\omega}}\mathbf{F}_{\mathrm{BB}}^{\hat{\omega}}[k]\right\|^2 \approx \sum_{i\in\{\mathrm{L,N}\}}\sum_{\hat{\omega}\in\Phi_{\mathrm{s},i}\setminus\hat{\mathbf{0}}}\frac{P_\mathrm{s}N_\mathrm{T}^\mathrm{s}\left(N_\mathrm{R}^\mathrm{s}\right)^2\widetilde{h}^{\hat{\mathbf{0}}\hat{\omega}}p_{\mathrm{BF}}(N_\mathrm{T}^\mathrm{s},N_\mathrm{R}^\mathrm{s},N_\mathrm{s})}{KN_\mathrm{s}R_{\hat{\omega}\hat{\mathbf{0}}}^{\alpha_{\mathrm{s},i}}}, \tag{8d}$$

where in (8a), $G_\mathrm{b}[k]$, $I_{\mathrm{m,b}}[k]$, and $I_{\mathrm{s,b}}[k]$ denote the power of the desired signal, the power of the interference from non-target gNBs, and that of the interference from IAB-nodes at subcarrier k, respectively; $0 < \eta < 1$ is the RSI controlling factor, which controls the amount of RSI; $\mathbb{E}\left\{\left|\left(\mathbf{w}_{\mathrm{RF}}^{\hat{\mathbf{0}}}\right)^H \mathbf{n}_\mathrm{b}[k]\right|^2\right\} = \sigma_\mathrm{n}^2 N_\mathrm{R}^\mathrm{s}$ is the Gaussian noise power with $\mathbf{n}_\mathrm{b}[k] \sim \mathcal{CN}(\mathbf{0}, \sigma_\mathrm{n}^2\mathbf{I}_{N_\mathrm{R}^\mathrm{s}})$; $\mathbb{E}\left\{|e_\mathrm{b}[k]|^2\right\}$ represents the quantization noise power owing to q bits ADC uniform quantization. In (8b)-(8d), $\widetilde{h}^{\hat{\mathbf{0}}\mathbf{x}_\mathrm{m}} = 10^{-0.1(\beta+\chi_\mathrm{m})}\left|h^{\hat{\mathbf{0}}\mathbf{x}_\mathrm{m}}\right|^2$, $\widetilde{h}^{\hat{\mathbf{0}}\omega} = 10^{-0.1(\beta+\chi_\mathrm{m})}\left|h^{\hat{\mathbf{0}}\omega}\right|^2$, and $\widetilde{h}^{\hat{\mathbf{0}}\hat{\omega}} = 10^{-0.1(\beta+\chi_{\mathrm{s},i})}\left|h^{\hat{\mathbf{0}}\hat{\omega}}\right|^2$ follow the composite GL distribution (see Appendix-A) because $\left|h^{(\cdot)}\right|^2$ is a Gamma distributed random variable[3]; $p_{\mathrm{ZF}}(N_\mathrm{T}^\mathrm{m}, N_\mathrm{m})$ is the ZF penalty, which is a Bernoulli random variable with success probability $(1-\frac{1}{N_\mathrm{T}^\mathrm{m}})^{N_\mathrm{m}-1}$ (see Remark 1); $p_{\mathrm{BF}}(N_\mathrm{T}^\mathrm{m}, N_\mathrm{R}^\mathrm{s}, N_\mathrm{m})$ and $p_{\mathrm{BF}}(N_\mathrm{T}^\mathrm{s}, N_\mathrm{R}^\mathrm{s}, N_\mathrm{s})$ are beamforming gains that take into account the sidelobe gains (see Proposition 1) because using the ON/OFF model given by the orthogonality of the steering vector can result in underestimation of the inter-cell interference as it gives zero beamforming gain when the azimuth and/or elevation angles are not the same. The approximation in (8b) is owing to the ZF penalty. The approximation in (8c) is obtained by assuming $\mathbf{F}_{\mathrm{BB}}^{\omega}[k] = \sqrt{\frac{N_\mathrm{T}^\mathrm{m}}{N_\mathrm{m}}}\mathbf{I}_{N_\mathrm{m}}$, where $\sqrt{\frac{N_\mathrm{T}^\mathrm{m}}{N_\mathrm{m}}}$ ensures $\left\|\mathbf{F}_{\mathrm{RF}}^{\omega}\mathbf{F}_{\mathrm{BB}}^{\omega}\right\|_F^2 = N_\mathrm{m}$. For a large number of antennas, the ZF penalty and the effect of the ZF on the inter-cell interference link can be neglected, as evaluated in [5], and (8d) follows a similar approximation.

Remark 1: For notation simplicity, we assume that the transmitter at $\mathbf{x}$ uses its 1st subarray to communicate with the typical receiver at $\mathbf{y}$. By adopting the orthogonality of the steering vector, given the transmit steering vector $\mathbf{a}_\mathrm{T}(\bar{\theta}_\mathrm{T}^{\mathbf{yx}}, \bar{\phi}_\mathrm{T}^{\mathbf{yx}})$, we have $\mathbf{a}_\mathrm{T}(\bar{\theta}_\mathrm{T}^{\mathbf{yx}}, \bar{\phi}_\mathrm{T}^{\mathbf{yx}})\mathbf{F}_{\mathrm{RF}}^{\mathbf{x}} = \left[\frac{\sqrt{N_\mathrm{T}^i}}{N_i}, 0, \ldots, 0\right] \in \mathbb{R}^{1\times N_i}$ only occurs when the AoD for the typical link is different from that for others served by the transmitter at $\mathbf{x}$, which has a probability of $\left(1-\frac{1}{N_\mathrm{T}^i}\right)^{N_i-1}$ for $p_{\mathrm{ZF}}(N_\mathrm{T}^i, N_i) = 1$. Accordingly, we have $\mathbf{f}_{\mathrm{BB},1}^{\mathbf{x}}[k] = \left[\sqrt{\frac{N_i}{N_\mathrm{T}^i}}, 0, \ldots, 0\right]^T$ satisfies $\left\|\mathbf{F}_{\mathrm{RF}}^{\mathbf{x}}\mathbf{f}_{\mathrm{BB},1}^{\mathbf{x}}[k]\right\|_F^2 = 1$. For a large number of antennas, other cases occur with very low probability, that is, $1-\left(1-\frac{1}{N_\mathrm{T}^i}\right)^{N_i-1}$, for tractability, the signal power is approximated to be 0 by setting $p_{\mathrm{ZF}}(N_\mathrm{T}^i, N_i) = 0$. Note that $i = \mathrm{m}$ denotes the transmitter at the gNB and $i = \mathrm{s}$ denotes that at the IAB-node [28].

Proposition 1: The beamforming gain (including sidelobe gains) of the inter-cell interference links is given by $p_{\mathrm{BF}}(N_\mathrm{T}^i, N_\mathrm{R}^j, N_i)$, which can be chosen from one of the values with the corresponding probability of occurrence in (9), as shown at the bottom of the next page, for $p, q \in \mathbb{N}$, $p+q \le N_i$, where $N_{\mathrm{T,x}}^i$ and $N_{\mathrm{T,y}}^i$ ($N_{\mathrm{R,x}}^j$ and $N_{\mathrm{R,y}}^j$) denote the number of antennas along x- and y-axis of the transmit (receive) UPA. $g_{\mathrm{T},i}$ and $\hat{g}_{\mathrm{T},i}$ ($g_{\mathrm{R},j}$ and $\hat{g}_{\mathrm{R},j}$) are the sidelobe gains at the transmitter (receiver). $i = \mathrm{m}$, $j = \mathrm{s}$; $i = \mathrm{s}$, $j = \mathrm{s}$; $i = \mathrm{m}$, $j = \mathrm{u}$; and $i = \mathrm{s}$, $j = \mathrm{u}$ denote the beamforming gain of the interference from gNBs to the typical IAB-node, IAB-nodes to the typical IAB-node, gNBs to the typical UE, and IAB-nodes to the typical UE, respectively.

Proof: Assume squared UPA, the inner product between transmit steering vectors is $\mathbf{a}_{\mathrm{T},i}^H(\bar{\theta}_1, \bar{\phi}_1)\mathbf{a}_{\mathrm{T},i}(\bar{\theta}_2, \bar{\phi}_2) =$

$$\begin{cases} 1 & \text{if } \bar{\theta}_1 = \bar{\theta}_2, \bar{\phi}_1 = \bar{\phi}_2 \\ g_{\mathrm{T},i} = \frac{1}{\sin^2(0.244)N_{\mathrm{T,x}}^i N_{\mathrm{T,y}}^i} & \text{if } \bar{\theta}_1 \neq \bar{\theta}_2, \bar{\phi}_1 \neq \bar{\phi}_2 \\ \hat{g}_{\mathrm{T},i} = \frac{1}{\sin(0.244)N_{\mathrm{T,x}}^i} & \text{otherwise,} \end{cases} \tag{10}$$

[3]If X is a Nakagami-M distributed random variable, then $X^2 \sim \mathrm{Gamma}(M, 1/M)$ is a unit mean Gamma-distributed random variable.

where the sidelobe gains $g_{\mathrm{T},i}$ and $\hat{g}_{\mathrm{T},i}$ are derived according to [37] and [5]. Similarly, we can model the inner product between the receiver steering vectors with sidelobe gains $g_{\mathrm{R},j}$ and $\hat{g}_{\mathrm{R},j}$. Recall that the virtual angles are uniformly distributed in their quantization sets, and according to the beamformer design in Section III-B, this proposition can be easily proven. ∎

According to [38], the ADC quantization noise power can be approximated as

$$\mathbb{E}\left\{|e_{\mathrm{b}}[k]|^2\right\} \approx \frac{1}{K}\sum_{k'=0}^{K-1}\frac{G_{\mathrm{b}}[k']+\eta_{\mathrm{dig}}\frac{\eta P_{\mathrm{s}}}{K}+I_{\mathrm{m,b}}[k']+I_{\mathrm{s,b}}[k']+\sigma_{\mathrm{n}}^2 N_{\mathrm{R}}^{\mathrm{s}}}{1.5\cdot 2^{2q}}, \tag{11}$$

where $\eta_{\mathrm{dig}} > 1$ is the amount of digital cancellation, introduced to reproduce the RSI power before the ADC (i.e., after analog SIC) because $\frac{\eta P_{\mathrm{s}}}{K}$ is the RSI power after the ADC (i.e., after digital SIC). q denotes the ADC quantization bits. Owing to Assumption 1, the value of the numerator of (11) is the same for all subcarriers. Thus, (11) can be simplified as

$$\mathbb{E}\left\{|e_{\mathrm{b}}[k]|^2\right\} \approx \frac{G_{\mathrm{b}}[k]+\eta_{\mathrm{dig}}\frac{\eta P_{\mathrm{s}}}{K}+I_{\mathrm{m,b}}[k]+I_{\mathrm{s,b}}[k]+\sigma_{\mathrm{n}}^2 N_{\mathrm{R}}^{\mathrm{s}}}{1.5\cdot 2^{2q}}. \tag{12}$$

2) ACCESS LINK

Next, assuming that gNB at $\mathbf{x}_{\mathrm{m}}$ uses its uth subarray to communicate with the typical UE at $\mathbf{0}$, we derive the SINR expression of the gNB-associated typical access link at subcarrier k, which is cast as

$$\mathrm{SINR}_{\mathbf{0}\mathbf{x}_{\mathrm{m}}}[k] = \frac{G_{\mathrm{a}}[k]}{I_{\mathrm{m,a}}[k]+I_{\mathrm{s,a}}[k]+\mathbb{E}\left\{\left|\left(\mathbf{w}_{\mathrm{RF}}^{\mathbf{0}}\right)^H \mathbf{n}_{\mathrm{a,m}}[k]\right|^2\right\}+\mathbb{E}\left\{|e_{\mathrm{a,m}}[k]|^2\right\}}, \tag{13a}$$

$$\begin{aligned} G_{\mathrm{a}}[k] &= \frac{P_{\mathrm{m}}}{KN_{\mathrm{m}}}\left|\left(\mathbf{w}_{\mathrm{RF}}^{\mathbf{0}}\right)^H \mathbf{H}_{\mathbf{0}\mathbf{x}_{\mathrm{m}}}[k]\mathbf{F}_{\mathrm{RF}}^{\mathbf{x}_{\mathrm{m}}}\mathbf{f}_{\mathrm{BB},u}^{\mathbf{x}_{\mathrm{m}}}[k]\right|^2 \\ &\approx \frac{P_{\mathrm{m}}N_{\mathrm{T}}^{\mathrm{m}}\left(N_{\mathrm{R}}^{\mathrm{u}}\right)^2\widetilde{h}^{\mathbf{0}\mathbf{x}_{\mathrm{m}}}p_{\mathrm{ZF}}(N_{\mathrm{T}}^{\mathrm{m}},N_{\mathrm{m}})}{KN_{\mathrm{m}}^2 R_{\mathbf{x}_{\mathrm{m}}\mathbf{0}}^{\alpha_{\mathrm{m}}}}, \end{aligned} \tag{13b}$$

$$\begin{aligned} I_{\mathrm{m,a}}[k] &= \frac{P_{\mathrm{m}}}{KN_{\mathrm{m}}}\left\|\sum_{\omega\in\Phi_{\mathrm{m}}\setminus\mathbf{x}_{\mathrm{m}}}\left(\mathbf{w}_{\mathrm{RF}}^{\mathbf{0}}\right)^H \mathbf{H}_{\mathbf{0}\omega}[k]\mathbf{F}_{\mathrm{RF}}^{\omega}\mathbf{F}_{\mathrm{BB}}^{\omega}[k]\right\|^2 \\ &\approx \sum_{\omega\in\Phi_{\mathrm{m}}\setminus\mathbf{x}_{\mathrm{m}}}\frac{P_{\mathrm{m}}N_{\mathrm{T}}^{\mathrm{m}}\left(N_{\mathrm{R}}^{u}\right)^2\widetilde{h}^{\mathbf{0}\omega}p_{\mathrm{BF}}(N_{\mathrm{T}}^{\mathrm{m}},N_{\mathrm{R}}^{\mathrm{u}},N_{\mathrm{m}})}{KN_{\mathrm{m}}R_{\omega\mathbf{0}}^{\alpha_{\mathrm{m}}}}, \end{aligned} \tag{13c}$$

$$\begin{aligned} I_{\mathrm{s,a}}[k] &= \sum_{i\in\{\mathrm{L,N}\}} I_{\mathrm{s,a}}^{i}[k] \\ &= \frac{P_{\mathrm{s}}}{KN_{\mathrm{s}}}\left\|\sum_{i\in\{\mathrm{L,N}\}}\sum_{\hat{\omega}\in\Phi_{\mathrm{s},i}\setminus\mathbf{0}}\left(\mathbf{w}_{\mathrm{RF}}^{\mathbf{0}}\right)^H \mathbf{H}_{\mathbf{0}\hat{\omega}}[k]\mathbf{F}_{\mathrm{RF}}^{\hat{\omega}}\mathbf{F}_{\mathrm{BB}}^{\hat{\omega}}[k]\right\|^2 \\ &\approx \sum_{i\in\{\mathrm{L,N}\}}\sum_{\hat{\omega}\in\Phi_{\mathrm{s},i}\setminus\mathbf{0}}\frac{P_{\mathrm{s}}N_{\mathrm{T}}^{\mathrm{s}}\left(N_{\mathrm{R}}^{\mathrm{u}}\right)^2\widetilde{h}^{\mathbf{0}\hat{\omega}}p_{\mathrm{BF}}(N_{\mathrm{T}}^{\mathrm{s}},N_{\mathrm{R}}^{\mathrm{u}},N_{\mathrm{s}})}{KN_{\mathrm{s}}R_{\hat{\omega}\mathbf{0}}^{\alpha_{\mathrm{s},i}}}, \end{aligned} \tag{13d}$$

where in (13a), $G_{\mathrm{a,m}}[k]$, $I_{\mathrm{m,a}}[k]$, and $I_{\mathrm{s,a}}[k]$ denote the power of the desired signal, that of the interference from non-target gNBs, and that of the interference from IAB-nodes at subcarrier k, respectively; $\mathbb{E}\left\{\left|\left(\mathbf{w}_{\mathrm{RF}}^{\mathbf{0}}\right)^H \mathbf{n}_{\mathrm{a,m}}[k]\right|^2\right\} = \sigma_{\mathrm{n}}^2 N_{\mathrm{R}}^{\mathrm{u}}$ is the Gaussian noise power with $\mathbf{n}_{\mathrm{a,m}}[k] \sim \mathcal{CN}(\mathbf{0}, \sigma_{\mathrm{n}}^2\mathbf{I}_{N_{\mathrm{R}}^{\mathrm{u}}})$; $\mathbb{E}\left\{\left|e_{\mathrm{a,m}}[k]\right|^2\right\}$ represents the ADC quantization noise power with a definition similar to that in (12). In (13b)-(13d), $\widetilde{h}^{\mathbf{0}\mathbf{x}_{\mathrm{m}}} = 10^{-0.1(\beta+\chi_{\mathrm{m}})}\left|h^{\mathbf{0}\mathbf{x}_{\mathrm{m}}}\right|^2$, $\widetilde{h}^{\mathbf{0}\omega} = 10^{-0.1(\beta+\chi_{\mathrm{m}})}\left|h^{\mathbf{0}\omega}\right|^2$, and $\widetilde{h}^{\mathbf{0}\hat{\omega}} = 10^{-0.1(\beta+\chi_{\mathrm{s},i})}\left|h^{\mathbf{0}\hat{\omega}}\right|^2$ follow from the composite GL distribution; $p_{\mathrm{ZF}}(N_{\mathrm{T}}^{\mathrm{m}}, N_{\mathrm{m}})$ is the ZF penalty following Remark 1; $p_{\mathrm{BF}}(N_{\mathrm{T}}^{\mathrm{m}}, N_{\mathrm{R}}^{\mathrm{u}}, N_{\mathrm{m}})$ and $p_{\mathrm{BF}}(N_{\mathrm{T}}^{\mathrm{s}}, N_{\mathrm{R}}^{\mathrm{u}}, N_{\mathrm{s}})$ are beamforming gains according to Proposition 1.

Finally, assuming the IAB-node at $\mathbf{x}_{\mathrm{s}}^{j}$ with $j \in \{\mathrm{L, N}\}$ uses its νth subcarrier to provide communications to the typical UE at $\mathbf{0}$, the SINR expression of the IAB-node associated typical access link at the subcarrier k is expressed as

$$\mathrm{SINR}_{\mathbf{0}\mathbf{x}_{\mathrm{s}}^{j}}[k] = \frac{G_{\mathrm{a,s}}[k]}{\hat{I}_{\mathrm{m,a}}[k]+\hat{I}_{\mathrm{s,a}}[k]+\mathbb{E}\left\{\left|\left(\mathbf{w}_{\mathrm{RF}}^{\mathbf{0}}\right)^H \mathbf{n}_{\mathrm{a,s}}[k]\right|^2\right\}+\mathbb{E}\left\{|e_{\mathrm{a,s}}[k]|^2\right\}} \tag{14a}$$

$$p_{\mathrm{BF}}(N_{\mathrm{T}}^{i}, N_{\mathrm{R}}^{j}, N_i) = \begin{cases} p+qg_{\mathrm{T},i}^2+(N_i-p-q)\hat{g}_{\mathrm{T},i}^2 & \text{w.p. } \frac{1}{N_{\mathrm{R}}^{j}}C_{N_i}^{p}C_{N_i-p}^{q}\left(\frac{1}{N_{\mathrm{T}}^{i}}\right)^p\left(1-\frac{1}{N_{\mathrm{T,x}}^{i}}-\frac{1}{N_{\mathrm{T,y}}^{i}}+\frac{1}{N_{\mathrm{T}}^{i}}\right)^{N_i-p-q} \\ & \quad\times\left(\frac{1}{N_{\mathrm{T,x}}^{i}}+\frac{1}{N_{\mathrm{T,y}}^{i}}-\frac{2}{N_{\mathrm{T}}^{i}}\right)^q \\ g_{\mathrm{R},j}^2\left[p+qg_{\mathrm{T},i}^2+(N_i-p-q)\hat{g}_{\mathrm{T},i}^2\right] & \text{w.p. } \left(1-\frac{1}{N_{\mathrm{R,x}}^{j}}-\frac{1}{N_{\mathrm{R,y}}^{j}}+\frac{1}{N_{\mathrm{R}}^{j}}\right)C_{N_i}^{p}C_{N_i-p}^{q}\left(\frac{1}{N_{\mathrm{T}}^{i}}\right)^p \\ & \quad\times\left(1-\frac{1}{N_{\mathrm{T,x}}^{i}}-\frac{1}{N_{\mathrm{T,y}}^{i}}+\frac{1}{N_{\mathrm{T}}^{i}}\right)^q\left(\frac{1}{N_{\mathrm{T,x}}^{i}}+\frac{1}{N_{\mathrm{T,y}}^{i}}-\frac{2}{N_{\mathrm{T}}^{i}}\right)^{N_i-p-q} \\ \hat{g}_{\mathrm{R},j}^2\left[p+qg_{\mathrm{T},i}^2+(N_i-p-q)\hat{g}_{\mathrm{T},i}^2\right] & \text{w.p. } \left(\frac{1}{N_{\mathrm{R,x}}^{j}}+\frac{1}{N_{\mathrm{R,y}}^{j}}-\frac{2}{N_{\mathrm{R}}^{j}}\right)C_{N_i}^{p}C_{N_i-p}^{q}\left(\frac{1}{N_{\mathrm{T}}^{i}}\right)^p \\ & \quad\times\left(1-\frac{1}{N_{\mathrm{T,x}}^{i}}-\frac{1}{N_{\mathrm{T,y}}^{i}}+\frac{1}{N_{\mathrm{T}}^{i}}\right)^q\left(\frac{1}{N_{\mathrm{T,x}}^{i}}+\frac{1}{N_{\mathrm{T,y}}^{i}}-\frac{2}{N_{\mathrm{T}}^{i}}\right)^{N_i-p-q} \end{cases}, \tag{9}$$

$$G_{\mathrm{a,s}}[k] = \frac{P_{\mathrm{s}}}{KN_{\mathrm{s}}}\left|\left(\mathbf{w}_{\mathrm{RF}}^{\mathbf{0}}\right)^{H}\mathbf{H}_{\mathbf{0}\mathbf{x}_{\mathrm{s}}^{j}}[k]\mathbf{F}_{\mathrm{RF}}^{\mathbf{x}_{\mathrm{s}}^{j}}\mathbf{f}_{\mathrm{BB},v}^{\mathbf{x}_{\mathrm{s}}^{j}}\right|^{2}$$
$$\approx \frac{P_{\mathrm{s}}N_{\mathrm{T}}^{\mathrm{s}}\left(N_{\mathrm{R}}^{\mathrm{u}}\right)^{2}\widetilde{h}^{\mathbf{0}\mathbf{x}_{\mathrm{s}}^{j}}p_{\mathrm{ZF}}(N_{\mathrm{T}}^{\mathrm{s}},N_{\mathrm{s}})}{KN_{\mathrm{s}}^{2}R_{\mathbf{x}_{\mathrm{s}}^{j}\mathbf{0}}^{\alpha_{\mathrm{s},j}}}, \tag{14b}$$

$$\hat{I}_{\mathrm{m,a}}[k] = \frac{P_{\mathrm{m}}}{KN_{\mathrm{m}}}\left\|\sum_{\omega\in\Phi_{\mathrm{m}}}\left(\mathbf{w}_{\mathrm{RF}}^{\mathbf{0}}\right)^{H}\mathbf{H}_{\mathbf{0}\omega}[k]\mathbf{F}_{\mathrm{RF}}^{\omega}\mathbf{F}_{\mathrm{BB}}^{\omega}\right\|^{2}$$
$$\approx \sum_{\omega\in\Phi_{\mathrm{m}}}\frac{P_{\mathrm{m}}N_{\mathrm{T}}^{\mathrm{m}}\left(N_{\mathrm{R}}^{\mathrm{u}}\right)^{2}\widetilde{h}^{\mathbf{0}\omega}p_{\mathrm{BF}}(N_{\mathrm{T}}^{\mathrm{m}},N_{\mathrm{R}}^{\mathrm{u}},N_{\mathrm{m}})}{KN_{\mathrm{m}}R_{\omega\mathbf{0}}^{\alpha_{\mathrm{m}}}}, \tag{14c}$$

$$\hat{I}_{\mathrm{s,a}}[k] = \sum_{i\in\{\mathrm{L,N}\}}\hat{I}_{\mathrm{s,a}}^{i}[k]$$
$$= \frac{P_{\mathrm{s}}}{KN_{\mathrm{s}}}\left\|\sum_{i\in\{\mathrm{L,N}\}}\sum_{\hat{\omega}\in\Phi_{\mathrm{s},i}\setminus\mathbf{x}_{\mathrm{s}}^{j}}\left(\mathbf{w}_{\mathrm{RF}}^{\mathbf{0}}\right)^{H}\mathbf{H}_{\mathbf{0}\hat{\omega}}[k]\mathbf{F}_{\mathrm{RF}}^{\hat{\omega}}\mathbf{F}_{\mathrm{BB}}^{\hat{\omega}}\right\|^{2}$$
$$\approx \sum_{i\in\{\mathrm{L,N}\}}\sum_{\hat{\omega}\in\Phi_{\mathrm{s},i}\setminus\mathbf{x}_{\mathrm{s}}^{j}}\frac{P_{\mathrm{s}}N_{\mathrm{T}}^{\mathrm{s}}\left(N_{\mathrm{R}}^{\mathrm{u}}\right)^{2}\widetilde{h}^{\mathbf{0}\hat{\omega}}p_{\mathrm{BF}}(N_{\mathrm{T}}^{\mathrm{s}},N_{\mathrm{R}}^{\mathrm{u}},N_{\mathrm{s}})}{KN_{\mathrm{s}}R_{\hat{\omega}\mathbf{0}}^{\alpha_{\mathrm{s},i}}}, \tag{14d}$$

where in (14a), $G_{\mathrm{a,s}}[k]$, $\hat{I}_{\mathrm{m,a}}[k]$, and $\hat{I}_{\mathrm{s,a}}[k]$ denote the power of the desired signal, that of the interference from gNBs, and that of the interference from non-target IAB-nodes at subcarrier k, respectively; $\mathbb{E}\left\{\left|\left(\mathbf{w}_{\mathrm{RF}}^{\mathbf{0}}\right)^{H}\mathbf{n}_{\mathrm{a,s}}[k]\right|^{2}\right\} = \sigma_{\mathrm{n}}^{2}N_{\mathrm{R}}^{\mathrm{u}}$ is the Gaussian noise power with $\mathbf{n}_{\mathrm{a,s}}[k] \sim \mathcal{CN}(\mathbf{0},\sigma_{\mathrm{n}}^{2}\mathbf{I}_{N_{\mathrm{R}}^{\mathrm{u}}})$; $\mathbb{E}\left\{\left|e_{\mathrm{a,s}}[k]\right|^{2}\right\}$ represents the ADC quantization noise power similar to (12). In (14b)-(14d), $\widetilde{h}^{\mathbf{0}\mathbf{x}_{\mathrm{s}}^{j}} = 10^{-0.1(\beta+\chi_{\mathrm{s},j})}\left|h^{\mathbf{0}\mathbf{x}_{\mathrm{s}}^{j}}\right|^{2}$, $\widetilde{h}^{\mathbf{0}\omega} = 10^{-0.1(\beta+\chi_{\mathrm{m}})}\left|h^{\mathbf{0}\omega}\right|^{2}$, and $\widetilde{h}^{\mathbf{0}\hat{\omega}} = 10^{-0.1(\beta+\chi_{\mathrm{s},i})}\left|h^{\mathbf{0}\hat{\omega}}\right|^{2}$ are composite GL distributed random variables; $p_{\mathrm{ZF}}(N_{\mathrm{T}}^{\mathrm{s}},N_{\mathrm{s}})$ is the ZF penalty following Remark 1; $p_{\mathrm{BF}}(N_{\mathrm{T}}^{\mathrm{m}},N_{\mathrm{R}}^{\mathrm{u}},N_{\mathrm{m}})$ and $p_{\mathrm{BF}}(N_{\mathrm{T}}^{\mathrm{s}},N_{\mathrm{R}}^{\mathrm{u}},N_{\mathrm{s}})$ are beamforming gains following Proposition 1.

V. PERFORMANCE ANALYSIS

For a standard OFDM system, owing to different channel gains occurring on different subcarriers, the effective SINR, whose statistics can be obtained by Lognormal or Gaussian approximations, is used to derive the performance metrics [39], [40], that is

$$\mathrm{SINR}_{eff} = \widetilde{\vartheta}\ln\left(\frac{1}{K}\sum_{k=0}^{K}e^{\frac{\mathrm{SINR}[k]}{\widetilde{\vartheta}}}\right), \tag{15}$$

where $\widetilde{\vartheta}$ is a parameter that depends on the coding scheme and number of coded bits in a block. However, in this work, thanks to Assumption 1, the value of SINR is the same for all subcarriers, which means $\mathrm{SINR}[k]\ \forall\ k$ equals to the effective SINR. Therefore, $\mathrm{SINR}[k]$ was utilized for the analysis, and the subcarrier index was omitted for simplicity.

A. ASSOCIATION PROBABILITIES

This subsection introduces the association probabilities; that is, the probabilities of a typical UE served by a gNB and an IAB-node, based on the maximum *long-term averaged biased-received-desired-signal power* (i.e., $\mathbb{E}\{\text{received-desired-signal power}\} \times$ bias factor T_i, for $i = \mathrm{m}$ if the desired signal comes from the gNB and $i = \mathrm{s}$ if it comes from the IAB-node) criteria [20]. The bias factor plays the role of offloading the traffic from gNB to IAB-node (or from IAB-node to gNB) to satisfy network-wide performance requirement [41]. The SINR coverage could be changed by tuning the bias ratio $\frac{T_{\mathrm{s}}}{T_{\mathrm{m}}}$, as shown in Section VI.

To derive the association probabilities, in the following lemmas, we first show the probability density function (PDF) and cumulative distribution function (CDF) of the contact distance (i.e., the distance of a typical point in a point process to its nearest point in an independent point process) for three different cases:

(i) The typical UE in PPP to its nearest LoS IAB-node in an independent PPP.
(ii) The typical UE in PPP to its nearest NLoS IAB-node in an independent PPP.
(iii) The typical UE in PPP to its nearest gNB in an independent MHCPP.

Lemma 1: The CDF of the contact distance from the PPP typical UE to the PPP LoS/NLoS IAB-node with density $\lambda_{\mathrm{s,L}}(x)/\lambda_{\mathrm{s,N}}(x)$ *is cast as*

$$F_{R_{\mathbf{x}_{\mathrm{s}}^{i}\mathbf{0}}}(r_{\mathrm{s},i}) = 1 - e^{-\int_{0}^{r_{\mathrm{s},i}}2\pi x\lambda_{\mathrm{s},i}(x)\mathrm{d}x}. \tag{16}$$

The corresponding PDF is written as

$$f_{R_{\mathbf{x}_{\mathrm{s}}^{i}\mathbf{0}}}(r_{\mathrm{s},i}) = 2\pi\lambda_{\mathrm{s},i}(r_{\mathrm{s},i})e^{-\int_{0}^{r_{\mathrm{s},i}}2\pi x\lambda_{\mathrm{s},i}(x)\mathrm{d}x}, \tag{17}$$

where $r_{\mathrm{s},i} > 0$ denotes the distance from the PPP typical UE to the PPP LoS IAB-node for $i = \mathrm{L}$; and that to the PPP NLoS IAB-node for $i = \mathrm{N}$.

Proof: The similar proof can be found in [42]. ■

Regarding the PDF and CDF of the PPP to MHCPP contact distance, it is impossible to obtain exact expressions because of the correlations among the MHCPP points. Fortunately, the authors in [43] provided a piece-wise model, as shown in the following lemma, which has been verified to provide a very close solution compared with the empirical data.

Lemma 2: The CDF of the contact distance from the PPP typical UE to the MHCPP gNB with density λ_{m} *and hard-core distance* ξ *is approximated as*

$$F_{R_{\mathbf{x}_{\mathrm{m}}\mathbf{0}}}(r_{\mathrm{m}}) = \begin{cases} F_{R_{\mathbf{x}_{\mathrm{m}}\mathbf{0}},1}(r_{\mathrm{m}}) = \pi\lambda_{\mathrm{m}}r_{\mathrm{m}}^{2} & 0 \le r_{\mathrm{m}} \le \frac{\xi}{2}, \\ F_{R_{\mathbf{x}_{\mathrm{m}}\mathbf{0}},2}(r_{\mathrm{m}}) = 1 - \frac{4-\pi\lambda_{\mathrm{m}}\xi^{2}}{4} & \\ \quad \times e^{\frac{2\pi\lambda_{\mathrm{m}}\xi^{2}\left[1-\left(\frac{2r_{\mathrm{m}}}{\xi}\right)^{\varrho}\right]}{\varrho\left(4-\pi\lambda_{\mathrm{m}}\xi^{2}\right)}} & r_{\mathrm{m}} > \frac{\xi}{2}. \end{cases} \tag{18}$$

Taking the first derivative with respect to r_{m}, we obtain the PDF of the contact distance as

$$f_{R_{\mathbf{x}_{\mathrm{m}}\mathbf{0}}}(r_{\mathrm{m}}) = \begin{cases} f_{R_{\mathbf{x}_{\mathrm{m}}\mathbf{0},1}}(r_{\mathrm{m}}) = 2\pi\lambda_{\mathrm{m}} r_{\mathrm{m}} & 0 \le r_{\mathrm{m}} \le \frac{\xi}{2}, \\ f_{R_{\mathbf{x}_{\mathrm{m}}\mathbf{0},2}}(r_{\mathrm{m}}) = 2\pi\lambda_{\mathrm{m}} r_{\mathrm{m}} \left(\frac{2r}{\xi}\right)^{\varrho-2} & \\ \quad \times e^{\frac{2\pi\lambda_{\mathrm{m}}\xi^2\left[1-\left(\frac{2r_{\mathrm{m}}}{\xi}\right)^{\varrho}\right]}{\varrho(4-\pi\lambda_{\mathrm{m}}\xi^2)}} & r_{\mathrm{m}} > \frac{\xi}{2}, \end{cases} \tag{19}$$

where $r_{\mathrm{m}} > 0$ denotes the distance from the PPP typical UE to MHCPP gNB; $\varrho \approx 0.3686(\lambda_{\mathrm{m}}\pi\xi^2)^2 + 0.0985\lambda_{\mathrm{m}}\pi\xi^2 + 2$ based on the simulation in [43].

Proof: A detailed proof can be found in [43]. ∎

Given the statistics of the contact distance, we now derive the probabilities of the typical UE associated with an LoS IAB-node, an NLoS IAB-node, and a gNB in the following propositions.

Proposition 2: The probability of a typical UE associated with an LoS/NLoS IAB-node at $\mathbf{x}_{\mathrm{s}}^{\mathrm{L}}/\mathbf{x}_{\mathrm{s}}^{\mathrm{N}}$, denoted as $A_{\mathrm{s,L}}/A_{\mathrm{s,N}}$, is expressed as:

$$\begin{aligned} A_{\mathrm{s},i} = &\int_0^{\left(\frac{\xi}{2\Delta_{i,1}}\right)^{\frac{\alpha_{\mathrm{m}}}{\alpha_{\mathrm{s},i}}}} \left(1 - F_{R_{\mathbf{x}_{\mathrm{m}}\mathbf{0},1}}\left(r_{\mathrm{s},i}^{\frac{\alpha_{\mathrm{s},i}}{\alpha_{\mathrm{m}}}} \Delta_{i,1}\right)\right) \\ &\times \left(1 - F_{R_{\mathbf{x}_{\mathrm{s}}^{j}\mathbf{0}}}\left(r_{\mathrm{s},i}^{\frac{\alpha_{\mathrm{s},i}}{\alpha_{\mathrm{s},j}}} \Delta_{i,2}\right)\right) f_{R_{\mathbf{x}_{\mathrm{s}}^{i}\mathbf{0}}}(r_{\mathrm{s},i}) \mathrm{d}r_{\mathrm{s},i} \\ &+ \int_{\left(\frac{\xi}{2\Delta_{i,1}}\right)^{\frac{\alpha_{\mathrm{m}}}{\alpha_{\mathrm{s},i}}}}^{\infty} \left(1 - F_{R_{\mathbf{x}_{\mathrm{m}}\mathbf{0},2}}\left(r_{\mathrm{s},i}^{\frac{\alpha_{\mathrm{s},i}}{\alpha_{\mathrm{m}}}} \Delta_{i,1}\right)\right) \\ &\times \left(1 - F_{R_{\mathbf{x}_{\mathrm{s}}^{j}\mathbf{0}}}\left(r_{\mathrm{s},i}^{\frac{\alpha_{\mathrm{s},i}}{\alpha_{\mathrm{s},j}}} \Delta_{i,2}\right)\right) f_{R_{\mathbf{x}_{\mathrm{s}}^{i}\mathbf{0}}}(r_{\mathrm{s},i}) \mathrm{d}r_{\mathrm{s},i}, \end{aligned} \tag{20}$$

where $i = \mathrm{L}$, $j = \mathrm{N}$; $i = \mathrm{N}$, $j = \mathrm{L}$. $\Delta_{i,1} = \left(\frac{P_{\mathrm{m}} N_{\mathrm{T}}^{\mathrm{m}} N_{\mathrm{s}}^2 T_{\mathrm{m}}}{P_{\mathrm{s}} N_{\mathrm{T}}^{\mathrm{s}} N_{\mathrm{m}}^2 T_{\mathrm{s}}}\right)^{\frac{1}{\alpha_{\mathrm{m}}}} e^{\frac{(0.1\zeta_{\mathrm{m}}\ln 10)^2 - (0.1\zeta_{\mathrm{s},i}\ln 10)^2}{2\alpha_{\mathrm{m}}}}$ and $\Delta_{i,2} = e^{\frac{(0.1\zeta_{\mathrm{s},j}\ln 10)^2 - (0.1\zeta_{\mathrm{s},i}\ln 10)^2}{2\alpha_{\mathrm{s},j}}}$. The integration bound is given by solving $r_{\mathrm{s},i}^{\frac{\alpha_{\mathrm{s},i}}{\alpha_{\mathrm{m}}}} \Delta_{i,1} = \frac{\xi}{2}$.

Proof: The proof can be found in Appendix-B. ∎

Proposition 3: The probability of a typical UE associated with a gNB at $\mathbf{x}_{\mathrm{m}}$, represented as A_{m}, is expressed as:

$$\begin{aligned} A_{\mathrm{m}} = &\int_0^{\frac{\xi}{2}} \left(1 - F_{R_{\mathbf{x}_{\mathrm{s}}^{\mathrm{L}}\mathbf{0}}}\left(r_{\mathrm{m}}^{\frac{\alpha_{\mathrm{m}}}{\alpha_{\mathrm{s,L}}}} \Delta_{\mathrm{L}}\right)\right) \\ &\times \left(1 - F_{R_{\mathbf{x}_{\mathrm{s}}^{\mathrm{N}}\mathbf{0}}}\left(r_{\mathrm{m}}^{\frac{\alpha_{\mathrm{m}}}{\alpha_{\mathrm{s,N}}}} \Delta_{\mathrm{N}}\right)\right) f_{R_{\mathbf{x}_{\mathrm{m}}\mathbf{0},1}}(r_{\mathrm{m}}) \mathrm{d}r_{\mathrm{m}} \\ &+ \int_{\frac{\xi}{2}}^{\infty} \left(1 - F_{R_{\mathbf{x}_{\mathrm{s}}^{\mathrm{L}}\mathbf{0}}}\left(r_{\mathrm{m}}^{\frac{\alpha_{\mathrm{m}}}{\alpha_{\mathrm{s,L}}}} \Delta_{\mathrm{L}}\right)\right) \\ &\times \left(1 - F_{R_{\mathbf{x}_{\mathrm{s}}^{\mathrm{N}}\mathbf{0}}}\left(r_{\mathrm{m}}^{\frac{\alpha_{\mathrm{m}}}{\alpha_{\mathrm{s,N}}}} \Delta_{\mathrm{N}}\right)\right) f_{R_{\mathbf{x}_{\mathrm{m}}\mathbf{0},2}}(r_{\mathrm{m}}) \mathrm{d}r_{\mathrm{m}}, \end{aligned} \tag{21}$$

where $\Delta_i = \left(\frac{P_{\mathrm{s}} N_{\mathrm{T}}^{\mathrm{s}} N_{\mathrm{m}}^2 T_{\mathrm{s}}}{P_{\mathrm{m}} N_{\mathrm{T}}^{\mathrm{m}} N_{\mathrm{s}}^2 T_{\mathrm{m}}}\right)^{\frac{1}{\alpha_{\mathrm{s},i}}} e^{\frac{(0.1\zeta_{s,i}\ln 10)^2 - (0.1\zeta_{m}\ln 10)^2}{2\alpha_{\mathrm{s},i}}}$ for $i \in \{\mathrm{L}, \mathrm{N}\}$.

Proof: The proof follows similar steps to Proposition 2 given the condition that the nearest gNB provides higher biased-received-desired-signal power than the nearest LoS and NLoS IAB-nodes. ∎

Having obtained the association probabilities, we can obtain the PDFs of the serving distance (i.e., the distance of the typical UE to its serving gNB or IAB-node) in the following proposition.

Proposition 4: Conditioned on the typical UE is served by its nearest gNB at $\mathbf{x}_{\mathrm{m}}$, and the corresponding PDF of the serving distance is written as

$$\begin{aligned} \hat{f}_{R_{\mathbf{x}_{\mathrm{m}}\mathbf{0}}}(r_{\mathrm{m}}) = &\frac{1}{A_{\mathrm{m}}} \left(1 - F_{R_{\mathbf{x}_{\mathrm{s}}^{\mathrm{L}}\mathbf{0}}}\left(r_{\mathrm{m}}^{\frac{\alpha_{\mathrm{m}}}{\alpha_{\mathrm{s,L}}}} \Delta_{\mathrm{L}}\right)\right) \\ &\times \left(1 - F_{R_{\mathbf{x}_{\mathrm{s}}^{\mathrm{N}}\mathbf{0}}}\left(r_{\mathrm{m}}^{\frac{\alpha_{\mathrm{m}}}{\alpha_{\mathrm{s,N}}}} \Delta_{\mathrm{N}}\right)\right) f_{R_{\mathbf{x}_{\mathrm{m}}\mathbf{0}}}(r_{\mathrm{m}}), \end{aligned} \tag{22}$$

where $f_{R_{\mathbf{x}_{\mathrm{m}}\mathbf{0}}}(r_{\mathrm{m}})$ is piece-wise at point $r_{\mathrm{m}} = \frac{\xi}{2}$ as stated in Lemma 2.

Similarly, conditioned on the typical UE being served by its nearest LoS (or NLoS) IAB-node at $\mathbf{x}_{\mathrm{s}}^{\mathrm{L}}$ (or $\mathbf{x}_{\mathrm{s}}^{\mathrm{N}}$), the corresponding PDF of the serving distance is given as

$$\begin{aligned} \hat{f}_{R_{\mathbf{x}_{\mathrm{s}}^{i}\mathbf{0}}}(r_{\mathrm{s},i}) = &\frac{1}{A_{\mathrm{s},i}} \left(1 - F_{R_{\mathbf{x}_{\mathrm{m}}\mathbf{0}}}\left(r_{\mathrm{s},i}^{\frac{\alpha_{\mathrm{s},i}}{\alpha_{\mathrm{m}}}} \Delta_{i,1}\right)\right) \\ &\times \left(1 - F_{R_{\mathbf{x}_{\mathrm{s}}^{j}\mathbf{0}}}\left(r_{\mathrm{s},i}^{\frac{\alpha_{\mathrm{s},i}}{\alpha_{\mathrm{s},j}}} \Delta_{i,2}\right)\right) f_{R_{\mathbf{x}_{\mathrm{s}}^{i}\mathbf{0}}}(r_{\mathrm{s},i}). \end{aligned} \tag{23}$$

When $i = \mathrm{L}$, we have $j = \mathrm{N}$; and when $i = \mathrm{N}$, we have $j = \mathrm{L}$. According to Lemma2, $F_{R_{\mathbf{x}_{\mathrm{m}}\mathbf{0}}}\left(r_{\mathrm{s},i}^{\frac{\alpha_{\mathrm{s},i}}{\alpha_{\mathrm{m}}}} \Delta_{i,1}\right)$ is piece-wise at point $r_{\mathrm{s},i} = \left(\frac{\xi}{2\Delta_{i,1}}\right)^{\frac{\alpha_{\mathrm{m}}}{\alpha_{\mathrm{s},i}}}$ by solving $r_{\mathrm{s},i}^{\frac{\alpha_{\mathrm{s},i}}{\alpha_{\mathrm{m}}}} \Delta_{i,1} = \frac{\xi}{2}$.

Proof: A simple proof can be found in [16, Lemma 4]. ∎

In the remaining subsections, we derive some performance metrics, such as SINR coverage, capacity with outage, and ergodic capacity for single-hop backhaul mmWave-IBFD/HD-IAB networks. We set the available bandwidth for IBFD communications as W. Assume that the HD transmission is in a frequency-division-duplexing (FDD) manner, whose available bandwidth is equally divided into two orthogonal portions (i.e., $W/2$): one for the gNB tier and the other for the IAB-node tier.

B. SINR COVERAGE

We first give the expression on the SINR coverage in the following theorem.

Theorem 1: The SINR coverage of the single-hop backhaul mmWave-IBFD-IAB network is defined as

$$\mathbb{P}_{\mathrm{FD}}(\tau) = A_{\mathrm{m}} \mathbb{P}\left(SINR_{\mathbf{0}\mathbf{x}_{\mathrm{m}}} > \tau\right)$$

$$+\sum_{i\in\{\mathrm{L},\mathrm{N}\}} A_{\mathrm{s},i}\mathbb{P}\left(SINR_{\mathbf{0}\mathbf{x}_{\mathrm{s}}^{i}}>\tau, SINR_{\mathbf{x}_{\mathrm{s}}^{i}\mathbf{x}_{\mathrm{m}}}>\tau\right), \tag{24}$$

where τ denotes the target SINR. $SINR_{\mathbf{x}_{\mathrm{s}}^{i}\mathbf{x}_{\mathrm{m}}}$ denotes the backhaul link SINR of the IAB-node at $\mathbf{x}_{\mathrm{s}}^{i}$ for serving a typical UE. However, solving $\mathbb{P}\left(SINR_{\mathbf{0}\mathbf{x}_{\mathrm{s}}^{i}}>\tau, SINR_{\mathbf{x}_{\mathrm{s}}^{i}\mathbf{x}_{\mathrm{m}}}>\tau\right)$ is intractable. Fortunately, since IAB-nodes and UEs are drawn from homogeneous PPP, according to Slivnyak's theorem, we have [16], [17]

$$\mathbb{P}\left(SINR_{\mathbf{0}\mathbf{x}_{\mathrm{s}}^{i}}>\tau, SINR_{\mathbf{x}_{\mathrm{s}}^{i}\mathbf{x}_{\mathrm{m}}}>\tau\right)=\mathbb{P}\left(SINR_{\mathbf{0}\mathbf{x}_{\mathrm{s}}^{i}}>\tau\right)\times\mathbb{P}\left(SINR_{\hat{\mathbf{0}}\mathbf{x}_{\mathrm{m}}}>\tau\right). \tag{25}$$

The solution of this theorem can be found in Appendix-D.

The SINR coverage of the single-hop backhaul mmWave-HD-IAB network $\mathbb{P}_{\mathrm{HD}}(\tau)$ can be derived similarly to Theorem 1; however, owing to the FDD, the interference from the other tier and the RSI in the SINR expressions should be removed. Moreover, the Gaussian noise power of HD is reduced by half compared to that of IBFD because the bandwidth of IBFD is twice as large as that of HD.

C. CAPACITY WITH OUTAGE

In the following theorem, we derive the expression on the capacity with outage.

Theorem 2: The capacity with outage, that is, the average rate correctly received over many transmission bursts, of the single-hop backhaul mmWave-IBFD-IAB network is cast as

$$\mathbb{C}_{\mathrm{FD}}(\tau_{\min})=W\log_2\left(1+\tau_{\min}\right)\mathbb{P}_{\mathrm{FD}}(\tau_{\min}), \tag{26}$$

where $\tau_{\min}$ is the minimum received SINR fixed at the transmitter because the transmitter does not know the instantaneous received SINR; thus, the transmission rate should be fixed independently.

Similarly, the capacity with outage of the single-hop backhaul mmWave-HD-IAB network $\mathbb{C}_{\mathrm{HD}}(\tau_{\min})$ is given by replacing W with $W/2$ and $\mathbb{P}_{\mathrm{FD}}(\tau_{\min})$ with $\mathbb{P}_{\mathrm{HD}}(\tau_{\min})$ in Theorem 2.

D. ERGODIC CAPACITY

The expression on the ergodic capacity is presented in the following theorem.

Theorem 3: The ergodic capacity for single-hop backhaul mmWave-IBFD-IAB networks, defined as the average of the instantaneous capacity, is written as

$$\mathbb{R}_{\mathrm{FD}}=A_{\mathrm{m}}\bar{\mathbb{R}}_{\mathrm{m}}+A_{\mathrm{s,L}}\min\left(\bar{\mathbb{R}}_{\mathrm{s,L}},\bar{\mathbb{R}}_{\mathrm{b}}\right)+A_{\mathrm{s,N}}\min\left(\bar{\mathbb{R}}_{\mathrm{s,N}},\bar{\mathbb{R}}_{\mathrm{b}}\right), \tag{27}$$

where $\bar{\mathbb{R}}_{\mathrm{m}}=\mathbb{E}\{W\log_2(1+SINR_{\mathbf{0}\mathbf{x}_{\mathrm{m}}})\}$, $\bar{\mathbb{R}}_{\mathrm{s,L}}=\mathbb{E}\{W\log_2(1+SINR_{\mathbf{0}\mathbf{x}_{\mathrm{s}}^{\mathrm{L}}})\}$, $\bar{\mathbb{R}}_{\mathrm{s,N}}=\mathbb{E}\{W\log_2(1+SINR_{\mathbf{0}\mathbf{x}_{\mathrm{s}}^{\mathrm{N}}})\}$ and $\bar{\mathbb{R}}_{\mathrm{b}}=\mathbb{E}\{W\log_2(1+SINR_{\hat{\mathbf{0}}\mathbf{x}_{\mathrm{m}}})\}$ represent ergodic capacities of the gNB associated access link, LoS IAB-node associated access link, NLoS IAB-node associated access link, and backhaul link, respectively, which are derived in Appendix-E.

Likewise, the ergodic capacity of the corresponding HD network $\mathbb{R}_{\mathrm{HD}}$ is given by scaling W in Theorem 3 with $1/2$ and removing the RSI and interference from the other tier in SINR expressions.

Note that we choose the minimum ergodic capacity between the IAB-node associated access link and the backhaul link as the final ergodic capacity at the UE associated with the IAB-node. This is because, in the IAB system, the maximum ergodic capacity that an IAB-node can provide is limited by its corresponding backhaul link [14], [17].

VI. NUMERICAL RESULTS

In this section, we verify the theoretical results derived in this study and evaluate the performance of the single-hop backhaul mmWave-IBFD-IAB networks. Furthermore, to better understand the advantages and disadvantages of IBFD transmission, comparisons are made between IBFD and HD schemes. Monte Carlo simulations with 10^6 iterations are performed to verify the accuracy of the derived theoretical results. Unless otherwise specified, the values of the simulation parameters are presented in Table 2.

A. ASSOCIATION PROBABILITIES AND SINR COVERAGE

Both figures in Fig. 2 show a close match between the simulation and analytical results, which indicates good accuracy given by our approximated analytical results derived in this study. In Fig. 2(a), we evaluate how the association probabilities can be affected by changing the bias ratio of the IAB-node to the gNB, that is, $\frac{T_{\mathrm{s}}}{T_{\mathrm{m}}}$. We can find that the association probability of a typical UE associates with an IAB-node, that is, A_{s}, increases as the ratio increases, and that of the typical UE associates with a gNB, that is, A_{m}, shows an opposite trend because as $\frac{T_{\mathrm{s}}}{T_{\mathrm{m}}}$ increases, more traffic is offloaded from the gNB to the IAB-node.

In Fig. 2(b), we study the impact of $\frac{T_{\mathrm{s}}}{T_{\mathrm{m}}}$ on SINR coverage. The SINR coverage at a fixed threshold first increases as $\frac{T_{\mathrm{s}}}{T_{\mathrm{m}}}$ increases; after reaching the maximum at $\frac{T_{\mathrm{s}}}{T_{\mathrm{m}}}=0$ dB, the SINR coverage decreases as the ratio increases. The reasons for this decrease are as follows. As $\frac{T_{\mathrm{s}}}{T_{\mathrm{m}}}$ increases, A_{s} becomes dominant, as shown in Fig. 2(a). Thus, according to Theorem 1, the SINR coverage of the network can be dominated by that of the IAB-node tier at a high bias ratio. Even if the gNB is tower-mounted, it has a direct fiber connection but a limited quantity owing to the high deployment cost of fiber-connected BSs. Biasing towards wireless IAB-nodes has the potential benefit of reducing deployment costs. However, because i) the transmit power and propagation properties of the IAB-node are worse than those of the gNB; ii) the performance of the IAB-node associated access link is restricted by the backhaul link, and iii) the backhaul link suffers from RSI, the network coverage becomes distorted. Moreover, it is interesting to note that the rate of increase in coverage is much lower than the decrement rate.

TABLE 2. System parameters and default values.

Notation	Physical Meaning	Values
K	Number of subcarriers	512 [44]
W	Bandwidth	800 MHz
f_c	Carrier frequency	38 GHz
$M_m, M_{s,L}, M_{s,N}$	Nakagami factor	4, 3, 2
σ_n^2	Gaussian noise power	-174 dBm $+ 10\log_{10} W + 10$ dB (IBFD) -174 dBm $+ 10\log_{10} \frac{W}{2} + 10$ dB (HD)
ϵ	Blockage density constant	0.0071 [19]
R_0	Radius of analysis region	1000m
ξ	Hard-core distance	100m
$\lambda_m, \lambda_s, \lambda_u$	gNB, IAB-node, and UE density	$1\times10^{-5}/\text{m}^2, 4\times10^{-5}/\text{m}^2, 2\times10^{-4}/\text{m}^2$
η	RSI controlling factor	80 dB [11]
η_{dig}	The amount of digital SIC	25 dB [11]
T	Gamma distribution samples	5 [29]
P_m, P_s	Transmit power	40 dBm, 33 dBm
T_s/T_m	Bias factor ratio	0 dB
N_m, N_s	Number of subarrays	8, 4
N_T^m, N_T^s	Number of transmit antennas	$32\times32, 16\times16$
N_R^s, N_R^u	Number of receive antennas	$16\times16, 8\times8$
$\alpha_m, \alpha_{s,L}, \alpha_{s,N}$	Path loss exponent	1.9, 2, 3.3 [45]
$\zeta_m, \zeta_{s,L}, \zeta_{s,N}$	Shadowing effect standard deviation	3.7, 4.3, 10.7 [45]
q	ADC quantization bits	8 bits
$\hat{g}_{T,m}, \hat{g}_{T,s}, g_{T,m}, g_{T,s}$	Transmitter sidelobe gain	-8.9 dB, -5.9 dB, -17.8 dB, -11.7 dB [5], [37]
$g_{R,s}, \hat{g}_{R,u}, g_{R,s}, g_{R,u}$	Receiver sidelobe gain	-5.9 dB, -2.9 dB, -11.7 dB, -5.7 dB [5], [37]

B. CAPACITY WITH OUTAGE

We assume that the transmitter fixes the minimum received SINR at $\tau_{\min} = 0$ dB. In Fig. 3(a), we compare the capacity with outage of single-hop backhaul mmWave-IBFD- and HD-IAB networks in terms of different bias ratios $\frac{T_s}{T_m}$ with various values of the RSI controlling factor η, which denotes the level of SIC (higher values denote poorer SIC). In general, as $\frac{T_s}{T_m}$ increases, the capacity with coverage decreases, which can be explained by Theorem 2 and the analysis in previous subsection. When $\eta > -50$ dB, the effect of the RSI on the capacity with outage becomes obvious. However, when $\eta > -20$ dB, the capacity with outage for different values of $\frac{T_s}{T_m}$ tends to be stable. This is because a high RSI makes the SINR coverage of the IAB-node tier approach 0; hence, the SINR coverage of the network is nearly dominated by that of the gNB tier. In addition, a trade-off between using IBFD and HD can be observed in the figure because the capacity with outage ratio of IBFD to HD decreased as η and/or $\frac{T_s}{T_m}$ increased. In some circumstances, HD can outperform the IBFD. For example, for $\frac{T_s}{T_m} = 20$ dB, HD provides a higher capacity with outage than IBFD when $\eta > -40$ dB. Interestingly, with efficient SIC, for $\frac{T_s}{T_m} = 0$ dB, using IBFD transmission can nearly double the capacity with outage compared to using HD; even if a high RSI is reserved, the capacity with outage of IBFD still outperforms that of HD. This is an attractive result because one can benefit from IBFD with high RSI power by tuning $\frac{T_s}{T_m}$ rather than exploring difficult and expensive SIC techniques to achieve higher levels of SIC. In addition, the capacity with outage ratio of IBFD to HD decreased as $\frac{T_s}{T_m}$ increased.

In Fig. 3(b), we also study how the capacity with outage of the single-hop backhaul mmWave-IBFD-IAB network is affected when using an ADC with different resolutions at various bias ratios at $\tau_{\min} = 0$ dB. Evidently, the capacity with outage can be improved by increasing the ADC quantization bits and reducing the bias ratio. Meanwhile, the capacity with outage saturates when the ADC resolution is higher than 5 bits, indicating that the ADC quantization noise effect becomes negligible compared to other interference and noise in our analyzed network. This result emphasizes the feasibility of using a low-resolution ADC in a network. Low-resolution ADCs are preferred in mmWave communications because their low power consumption can compensate for the high power consumption imposed by numerous RF chains [46].

The simulation results for verifying the analytical results of capacity with outage are omitted because they depend on the SINR coverage, which shows a close match between the simulation and analytical results in Fig. 2(b).

C. ERGODIC CAPACITY

Fig. 4 compares the network ergodic capacity with varying RSI factor η and hard-core distance ξ between single-hop backhaul FR2-IBFD- and HD-IAB networks in terms of different density ratios of the IAB-node to gNB $\frac{\lambda_s}{\lambda_m}$. Fig. 4(a) shows how the RSI affects the network ergodic capacity. Note that when $\frac{\lambda_s}{\lambda_m}$ increases, the effective cell radius of the IAB-node tier decreases, resulting in a higher ergodic capacity of the corresponding link. In contrast, the ergodic capacity of the gNB tier is reduced because the UEs are more likely to be served by the IAB-nodes as $\frac{\lambda_s}{\lambda_m}$ increases. When $\eta \leq -50$ dB, the ergodic capacity increment of the IAB-node tier is higher than the decrement of the gNB tier as the ratio increases. Thus, the overall ergodic capacity increases as the ratio increases. However, for $\eta > -50$ dB, the growth in the ergodic capacity of the IAB-node tier is less than that of the gNB tier as the ratio increases; hence, the overall ergodic capacity decreases as the ratio increases. This result indicates that with successful SIC, the network ergodic capacity can be improved by increasing $\frac{\lambda_s}{\lambda_m}$. Compared with HD transmission, if $\eta \leq -50$ dB, the ergodic capacity provided by the IBFD scheme is around 1.6 times higher than that provided by

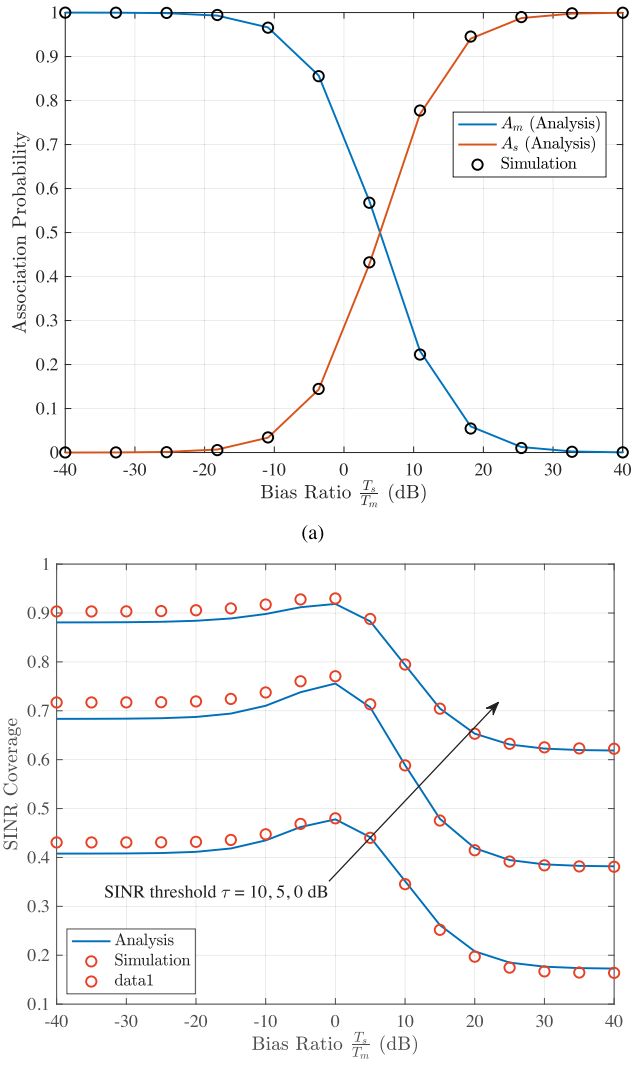

FIGURE 2. Verification of theoretical results for (a) association probabilities and (b) SINR coverage v.s. bias ratio $\frac{T_s}{T_m}$ at SINR threshold $\tau = 0, 5, 10$ dB.

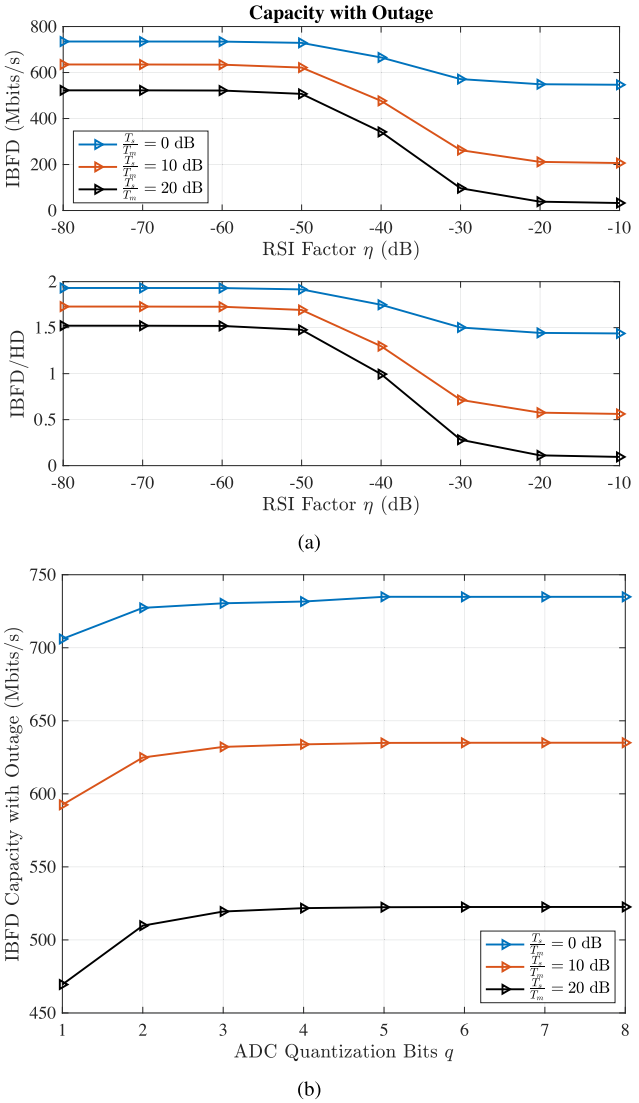

FIGURE 3. Single-hop backhaul mmWave-IBFD-IAB networks capacity with outage at a minimum received SINR = 0 dB (i.e., $\tau_{\min} = 0$ dB) in terms of $\frac{T_s}{T_m} = 0, 10, 20$ dB (a) v.s. different values of RSI factors; (b) v.s. different values of ADC quantization bits.

HD transmission, regardless of the density ratio. However, in the high RSI factor η region, the higher the density ratio, the lower the ergodic capacity provided by the IBFD, and thus, the lower the ergodic capacity ratio of IBFD to HD $\frac{\mathbb{R}_{\text{FD}}}{\mathbb{R}_{\text{HD}}}$ is. Moreover, a similar trade-off between using HD and IBFD, as shown in Fig. 3(a), can be concluded here, i.e., the ergodic capacity of HD can outperform IBFD for a high $\frac{\lambda_s}{\lambda_m}$ and/or high η. Since the close match between the simulation and analytical results is shown in the figure, which indicates good accuracy given by our analytical results derived for the network ergodic capacity.

In Fig. 4(b), by fixing the density of the gNB, the interference given by the gNBs is suppressed by increasing the hard-core distance ξ, and as ξ increases, the network ergodic capacity increases, which is the case for both the IBFD and HD schemes. In particular, as ξ increases, the IBFD ergodic capacity gap between different node density ratios is reduced. Interestingly, when ξ is equal to 0, MHCPP converges to PPP, which yields the lowest ergodic capacity. This result highlights the necessity of imposing a suitable distance between the gNBs. Moreover, with successful SIC, IBFD provides a higher ergodic capacity than HD, regardless of ξ is. The simulation results are omitted here because the accuracy of our analytical results on the network ergodic capacity is verified in Fig. 4(a).

D. EFFECT OF ASSUMPTION 1

In Fig. 5, we simulate the ergodic capacity for different links per subcarrier to analyze the effect of Assumption 1 by simulations and provide the corresponding ergodic capacity for the multi-path scenario with three paths for both the LoS and NLoS. For the multi-path scenario, we relax Assumption 1, and the power of the desired signal is calculated based on Lemma 1 in [5]. This lemma states that for a large number of antennas, when the number of paths is much smaller than

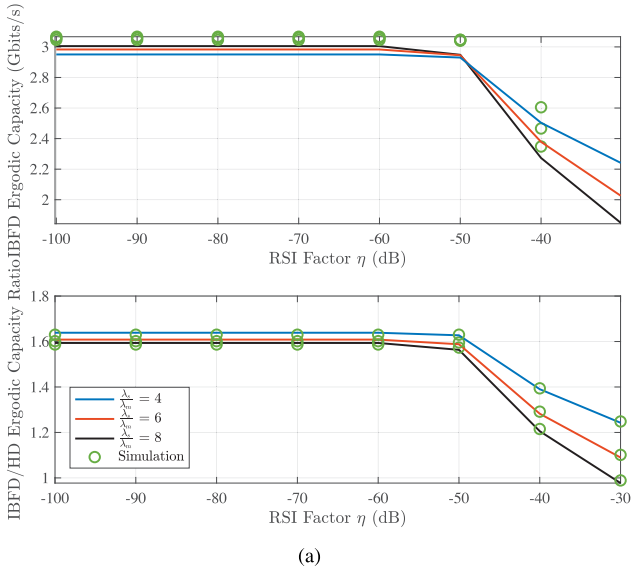

(a)

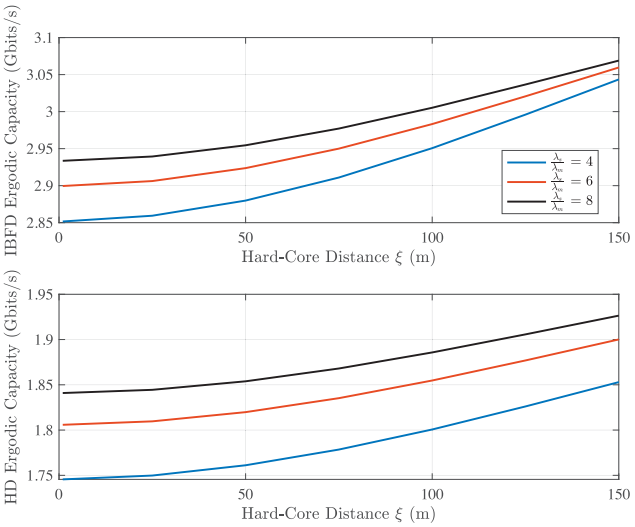

(b)

FIGURE 4. Single-hop backhaul mmWave-IBFD-IAB networks ergodic capacity in terms of $\frac{\lambda_s}{\lambda_m} = 4, 6, 8$ ($\lambda_m = 1 \times 10^{-5}/m^2$) (a) v.s. different RSI factor; (b) v.s. different hard-core distance.

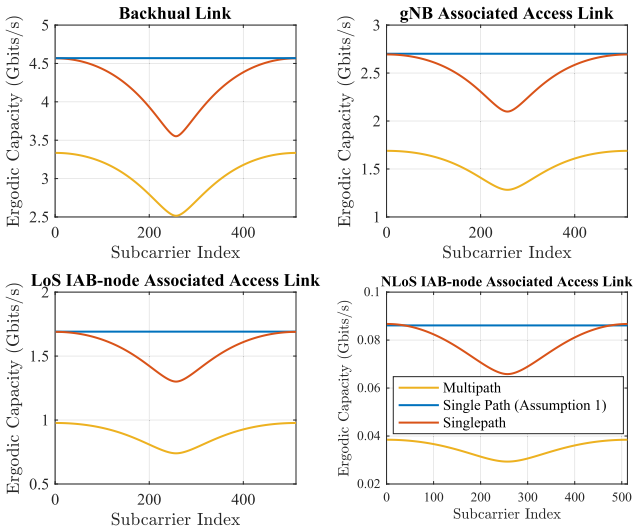

FIGURE 5. Ergodic capacity comparison for different links per subcarrier in terms of single path and multi-path scenario.

the number of antennas, the power of the desired signal converges to the power given by the strongest path, where the optimal RF beamformers are given by the AoA and AoD of the strongest path. With Assumption 1, the single path channel is assumed to exhibit flat fading, that is, the channel gain is the same for all subcarriers. Therefore, we obtain a constant ergodic capacity across all subcarriers. By relaxing Assumption 1, $\gamma[k]$ in (4) varies for each subcarrier, which gives us the concave curves in Fig. 5. It can be seen that Assumption 1 is a strong assumption, which gives us an upper band on ergodic capacity. Without Assumption 1, the performance analyzed in the previous subsections is degraded. Moreover, by adding a multi-path to the picture, we can observe further degradation of ergodic capacity. This is because multi-path propagation introduces additional interference, which reduces the SINR compared with that in the single path scenario. However, even if Assumption 1 is a strong assumption, it provides tractability in stochastic geometry analysis for OFDM modulation, because the statistics of raised cosine pulse shaping filters are still unknown in the literature and are difficult to derive owing to the complex impulse response of the filter [47], [48].

VII. CONCLUSION

In this study, the performance of multi-cell wideband single-hop backhaul mmWave-IBFD-IAB networks using stochastic geometry, where the gNBs are deployed in MHCPP, was investigated. For the Nakagami-M small fading and log-normal shadowing effect, we leveraged the approximated composite GL distribution for network performance analysis. Moreover, for simplicity, the PGFL of PPP was adopted to approximate the mean interference given by the gNBs. Consequently, our closed-form performance metrics showed a close match with the simulations. Furthermore, comparisons were made with the performance of the single-hop backhaul mmWave-HD-IAB networks. The numerical results demonstrated that tuning the bias ratio of the IAB-node to gNB, the SINR coverage at a fixed SINR threshold shows a convex trend. Interestingly, we found that by selecting a suitable bias ratio, the IBFD scheme can always perform better than HD, even with a high RSI power, relaxing the requirement for high-quality SIC techniques. Moreover, at SINR $=$ 0 dB, the effect of ADC quantization noise can be neglected at a lower resolution. As for the network ergodic capacity, fixing the density of gNB, the ergodic capacity was enhanced by deploying gNBs with MHCPP compared to deploying gNBs with PPP, emphasizing the advantage of utilizing MHCPP. Moreover, the larger the hard-core distance, the higher the ergodic capacity. Additionally, with a small RSI power, the ergodic capacity can be improved by increasing the ratio of the density of the IAB-node to gNB.

Further work can be focused on determing the transformation properties of the MHCPP and deriving the system performance with the impact of hardware impairments and channel estimation error. Moreover, the design and analysis of a multi-hop backhaul scenario are worth studying.

APPENDIX A
COMPOSITE GAMMA-LOGNORMAL DISTRIBUTION

Given that $X \sim \text{Gamma}(M, 1/M)$ and $Y \sim \ln\mathcal{N}(\hat{\mu}, \hat{\sigma}^2)$ are independent Gamma and Lognormal distributed random variables, respectively, then $Z = XY \sim GL(M, \frac{1}{M}, \hat{\mu}, \hat{\sigma}^2)$ is defined as a composite GL distributed random variable with $\mathbb{E}\{Z\} = e^{\hat{\mu}+0.5\hat{\sigma}^2}$. As the exact PDF is intractable for deriving the corresponding CDF and Laplace transform, a good approximation is provided by [29, Lemma 1].

The corresponding approximated CDF is given as

$$F_Z(z) \approx \frac{1}{\Gamma(M)\sum_{t=1}^{T} w_t} \sum_{t=1}^{T} w_t \gamma\left(M, zMe^{-(\sqrt{2}\hat{\sigma}v_t+\hat{\mu})}\right), \quad (28)$$

where $\gamma(s,x) = \int_0^x t^{s-1}e^{-t}\mathrm{d}t$ is the incomplete gamma function. T, w_t, and v_t are the number of gamma distribution samples, weight, and abscissas factors for the Gaussian-Hermite integration, respectively, whose values can be obtained from [49].

The Laplace transform is approximated as

$$\mathscr{L}_Z(s) = \mathbb{E}\left\{e^{-sz}\right\} \approx \frac{1}{\sum_{t=1}^{T} w_t} \sum_{t=1}^{T} \frac{w_t M^M e^{-M(\sqrt{2}\hat{\sigma}v_t+\hat{\mu})}}{\left(s+Me^{-(\sqrt{2}\hat{\sigma}v_t+\hat{\mu})}\right)^M}. \quad (29)$$

APPENDIX B
PROOF OF PROPOSITION 2

A typical UE is associated with its nearest LoS IAB-node rather than the nearest gNB and NLoS IAB-node if the nearest LoS IAB-node can provide the highest long-term averaged biased-received-desired-signal power, given as

$$\begin{aligned}
A_{\mathrm{s,L}} &= \mathbb{P}\left(\frac{P_{\mathrm{s}}N_{\mathrm{T}}^{\mathrm{s}}(N_{\mathrm{R}}^{\mathrm{u}})^2T_{\mathrm{s}}}{KN_{\mathrm{s}}^2}\mathbb{E}\left\{\widetilde{h}^{\mathbf{0}\mathbf{x}_{\mathrm{s}}^{\mathrm{L}}}\right\}R_{\mathbf{x}_{\mathrm{s}}^{\mathrm{L}}\mathbf{0}}^{-\alpha_{\mathrm{s,L}}} \geq \frac{P_{\mathrm{m}}N_{\mathrm{T}}^{\mathrm{m}}(N_{\mathrm{R}}^{\mathrm{u}})^2T_{\mathrm{m}}}{KN_{\mathrm{m}}^2}\right.\\
&\quad\times\mathbb{E}\left\{\widetilde{h}^{\mathbf{0}\mathbf{x}_{\mathrm{m}}}\right\}R_{\mathbf{x}_{\mathrm{m}}\mathbf{0}}^{-\alpha_{\mathrm{m}}} \bigcap \frac{P_{\mathrm{s}}N_{\mathrm{T}}^{\mathrm{s}}(N_{\mathrm{R}}^{\mathrm{u}})^2T_{\mathrm{s}}}{KN_{\mathrm{s}}^2}\mathbb{E}\left\{\widetilde{h}^{\mathbf{0}\mathbf{x}_{\mathrm{s}}^{\mathrm{L}}}\right\}R_{\mathbf{x}_{\mathrm{s}}^{\mathrm{L}}\mathbf{0}}^{-\alpha_{\mathrm{s,L}}}\\
&\quad\left.\geq \frac{P_{\mathrm{s}}N_{\mathrm{T}}^{\mathrm{s}}(N_{\mathrm{R}}^{\mathrm{u}})^2T_{\mathrm{s}}}{KN_{\mathrm{s}}^2}\mathbb{E}\left\{\widetilde{h}^{\mathbf{0}\mathbf{x}_{\mathrm{s}}^{\mathrm{N}}}\right\}R_{\mathbf{x}_{\mathrm{s}}^{\mathrm{N}}\mathbf{0}}^{-\alpha_{\mathrm{s,N}}}\right)\\
&\overset{(a)}{=}\mathbb{P}\left(\frac{P_{\mathrm{s}}N_{\mathrm{T}}^{\mathrm{s}}(N_{\mathrm{R}}^{\mathrm{u}})^2T_{\mathrm{s}}}{KN_{\mathrm{s}}^2}e^{-0.1\beta\ln 10+\frac{(0.1\zeta_{\mathrm{s,L}}\ln 10)^2}{2}}R_{\mathbf{x}_{\mathrm{s}}^{\mathrm{L}}\mathbf{0}}^{-\alpha_{\mathrm{s,L}}} \geq R_{\mathbf{x}_{\mathrm{m}}\mathbf{0}}^{-\alpha_{\mathrm{m}}}\right.\\
&\quad\times\frac{P_{\mathrm{m}}N_{\mathrm{T}}^{\mathrm{m}}(N_{\mathrm{R}}^{\mathrm{u}})^2T_{\mathrm{m}}}{KN_{\mathrm{m}}^2}e^{-0.1\beta\ln 10+\frac{(0.1\zeta_{\mathrm{m}}\ln 10)^2}{2}}\bigcap\frac{P_{\mathrm{s}}N_{\mathrm{T}}^{\mathrm{s}}(N_{\mathrm{R}}^{\mathrm{u}})^2T_{\mathrm{s}}}{KN_{\mathrm{s}}^2}\\
&\quad\times e^{-0.1\beta\ln 10+\frac{(0.1\zeta_{\mathrm{s,L}}\ln 10)^2}{2}}R_{\mathbf{x}_{\mathrm{s}}^{\mathrm{L}}\mathbf{0}}^{-\alpha_{\mathrm{s,L}}} \geq \frac{P_{\mathrm{s}}N_{\mathrm{T}}^{\mathrm{s}}(N_{\mathrm{R}}^{\mathrm{u}})^2T_{\mathrm{s}}}{KN_{\mathrm{s}}^2}R_{\mathbf{x}_{\mathrm{s}}^{\mathrm{N}}\mathbf{0}}^{-\alpha_{\mathrm{s,N}}}\\
&\quad\left.\times e^{-0.1\beta\ln 10+\frac{(0.1\zeta_{\mathrm{s,N}}\ln 10)^2}{2}}\right)\\
&\overset{(b)}{=}\int_0^{\infty}\mathbb{P}\left(R_{\mathbf{x}_{\mathrm{m}}\mathbf{0}} \geq r_{\mathrm{s,L}}^{\frac{\alpha_{\mathrm{s,L}}}{\alpha_{\mathrm{m}}}}\Delta_{\mathrm{L},1}\right)\mathbb{P}\left(R_{\mathbf{x}_{\mathrm{s}}^{\mathrm{N}}\mathbf{0}} \geq r_{\mathrm{s,L}}^{\frac{\alpha_{\mathrm{s,L}}}{\alpha_{\mathrm{s,N}}}}\Delta_{\mathrm{L},2}\right)\\
&\quad\times f_{R_{\mathbf{x}_{\mathrm{s}}^{\mathrm{L}}\mathbf{0}}}(r_{\mathrm{s,L}})\mathrm{d}r_{\mathrm{s,L}}, \quad (30)
\end{aligned}$$

where (a) is derived by substituting the mean power of the composite fading. (b) is obtained by taking the average of $R_{\mathbf{x}_{\mathrm{s}}^{\mathrm{L}}\mathbf{0}} = r_{\mathrm{s,L}}$. By using Lemma 1 and Lemma 2, we can complete the proof. The proof of $A_{\mathrm{s,N}}$ can be provided in a similar manner.

APPENDIX C
A USEFUL LEMMA

A useful lemma shown below can support the derivation of SINR coverage. With the following lemma, one can easily deploy the PGFL of PPP to estimate the mean interference from gNBs in the backhaul link and the gNB-associated access link.

Lemma 3: Given the density of the MHCPP gNB as λ_{m} with hard-core distance ξ, it can be approximated by thinning the density of its parent PPP $\widetilde{\lambda}_{\mathrm{m}}$ with $\rho_{\mathrm{M}}(r_0)$, where $\rho_{\mathrm{M}}(r_0)$ is the conditional thinning Palm probability with $r_0 > 0$ being the distance between the two gNBs, which is expressed as

$$\rho_{\mathrm{M}}(r_0) = \begin{cases} \frac{2}{\widetilde{\lambda}_{\mathrm{m}}(\kappa-\pi\xi^2)}\left[1-\frac{\pi\xi^2\widetilde{\lambda}_{\mathrm{m}}\left(1-e^{-\widetilde{\lambda}_{\mathrm{m}}\kappa}\right)}{\widetilde{\lambda}_{\mathrm{m}}\kappa\left(1-e^{-\pi\xi^2\widetilde{\lambda}_{\mathrm{m}}}\right)}\right] & \xi \leq r_0 < 2\xi\\ \rho & r_0 \geq 2\xi\\ 0 & \textit{otherwise}, \end{cases} \quad (31)$$

with $\kappa = 2\pi\xi^2 - 2\xi^2 cos^{-1}\left(\frac{r_0}{2\xi}\right) + r_0\sqrt{\xi^2-\frac{r_0^2}{4}}$.

Proof: A proof can be found in [23]. ■

APPENDIX D
SOLUTION OF THEOREM 1

A. SOLUTION OF $\mathbb{P}\left(SINR_{\mathbf{0}\mathbf{x}_{\mathrm{s}}^{\mathrm{L}}} > \tau\right)$

The SINR coverage for the LoS IAB-node associated access link is expressed as

$$\begin{aligned}
&\mathbb{P}\left(\mathrm{SINR}_{\mathbf{0}\mathbf{x}_{\mathrm{s}}^{\mathrm{L}}} > \tau\right)\\
&= \left(1-\tfrac{1}{N_{\mathrm{T}}^{\mathrm{s}}}\right)^{N_{\mathrm{s}}-1}\int_0^{R_0}\mathbb{P}\left(\widetilde{h}^{\mathbf{0}\mathbf{x}_{\mathrm{s}}^{\mathrm{L}}} > \mathcal{G}_{\mathrm{s}}\right.\\
&\quad\left.\times\underbrace{r_{\mathrm{s,L}}^{\alpha_{\mathrm{s,L}}}\left(\hat{I}_{\mathrm{m,a}}+\hat{I}_{\mathrm{s,a}}^{\mathrm{L}}+\hat{I}_{\mathrm{s,a}}^{\mathrm{N}}+\sigma_{\mathrm{n}}^2N_{\mathrm{R}}^{\mathrm{u}}\right)}_{I}\right)\hat{f}_{R_{\mathbf{x}_{\mathrm{s}}^{\mathrm{L}}\mathbf{0}}}(r_{\mathrm{s,L}})\mathrm{d}r_{\mathrm{s,L}}\\
&\overset{(a)}{\approx}\left(1-\tfrac{1}{N_{\mathrm{T}}^{\mathrm{s}}}\right)^{N_{\mathrm{s}}-1}\int_0^{R_0}\left[1-\mathbb{E}\left\{\frac{1}{\Gamma(M_{\mathrm{s,L}})\sum_{t=1}^{T}w_t}\sum_{t=1}^{T}w_t\right.\right.\\
&\quad\left.\left.\times\ \gamma\left(M_{\mathrm{s,L}}, \mathcal{G}_{\mathrm{s},t}I\right)\right\}\right]\hat{f}_{R_{\mathbf{x}_{\mathrm{s}}^{\mathrm{L}}\mathbf{0}}}(r_{\mathrm{s,L}})\mathrm{d}r_{\mathrm{s,L}}\\
&\overset{(b)}{=}\left(1-\tfrac{1}{N_{\mathrm{T}}^{\mathrm{s}}}\right)^{N_{\mathrm{s}}-1}\sum_{t=1}^{T}\sum_{n=0}^{M_{\mathrm{s,L}}-1}\frac{w_t}{n!\sum_{t=1}^{T}w_t}\\
&\quad\times\int_0^{R_0}\mathbb{E}\left\{\left(\mathcal{G}_{\mathrm{s},t}I\right)^n e^{-\mathcal{G}_{\mathrm{s},t}I}\right\}\hat{f}_{R_{\mathbf{x}_{\mathrm{s}}^{\mathrm{L}}\mathbf{0}}}(r_{\mathrm{s,L}})\mathrm{d}r_{\mathrm{s,L}}
\end{aligned}$$

$$= \left(1-\frac{1}{N_{\mathrm{T}}^{\mathrm{s}}}\right)^{N_{\mathrm{s}}-1} \sum_{t=1}^{T} \sum_{n=0}^{M_{\mathrm{s,L}}-1} \frac{w_t(-\mathcal{G}_{\mathrm{s},t})^n}{n!\sum_{t=1}^{T} w_t} \frac{\mathrm{d}^n}{\mathrm{d}\mathcal{G}_{\mathrm{s},t}^n} \times \left(\int_0^{R_0} \mathbb{E}\left\{ e^{-\mathcal{G}_{\mathrm{s},t} r_{\mathrm{s,L}}^{\alpha_{\mathrm{s,L}}} \hat{I}_{\mathrm{s,a}}^{\mathrm{L}}} \right\} \mathbb{E}\left\{ e^{-\mathcal{G}_{\mathrm{s},t} r_{\mathrm{s,L}}^{\alpha_{\mathrm{s,L}}} \hat{I}_{\mathrm{s,a}}^{\mathrm{N}}} \right\} \times \mathbb{E}\left\{ e^{-\mathcal{G}_{\mathrm{s},t} r_{\mathrm{s,L}}^{\alpha_{\mathrm{s,L}}} \hat{I}_{\mathrm{m,a}}} \right\} e^{-\mathcal{G}_{\mathrm{s},t} r_{\mathrm{s,L}}^{\alpha_{\mathrm{s,L}}} \sigma_{\mathrm{n}}^2 N_{\mathrm{R}}^{\mathrm{u}}} \hat{f}_{R_{\mathbf{x}_{\mathrm{s}}^{\mathrm{L}}\mathbf{0}}}(r_{\mathrm{s,L}}) \mathrm{d}r_{\mathrm{s,L}} \right), \tag{32}$$

where $\mathcal{G}_{\mathrm{s}} = \frac{\tau K N_{\mathrm{s}}^2 \left(1+\frac{1}{1.5\cdot 2^{2q}}\right)}{P_{\mathrm{s}} N_{\mathrm{T}}^{\mathrm{s}} (N_{\mathrm{R}}^{\mathrm{u}})^2 \left(1-\frac{\tau}{1.5\cdot 2^{2q}}\right)}$. $\mathcal{G}_{\mathrm{s},t} = \mathcal{G}_{\mathrm{s}} M_{\mathrm{s,L}} e^{-(\sqrt{2}\hat{\sigma}_{\mathrm{s,L}}\nu_t + \hat{\mu})}$ with $\hat{\mu} = -0.1\beta \ln 10$ and $\hat{\sigma}_{\mathrm{s,L}} = 0.1\zeta_{\mathrm{s,L}} \ln 10$. (a) is derived from the approximated CDF of the composite GL distribution and (b) can be referred to [50, Eq.(8.4.8)].

Next, we present the mean interference from LoS IAB-nodes in (33), as shown at the bottom of the page, where (c) is derived according to the approximated Laplace transform of the composite GL distribution. After applying the PGFL of PPP, we obtain (d). In (e), we explore the independence of different beamforming gain scenarios, b_i takes one of the beamforming gains from (9), and c_i takes the corresponding probability.

Then, the mean interference from NLoS IAB-nodes $\mathbb{E}\left\{ e^{-\mathcal{G}_{\mathrm{s},t} r_{\mathrm{s,L}}^{\alpha_{\mathrm{s,L}}} \hat{I}_{\mathrm{s,a}}^{\mathrm{N}}} \right\}$ can be obtained by a similar step in (33) with integration from $r_{\mathrm{s,L}}^{\frac{\alpha_{\mathrm{s,L}}}{\alpha_{\mathrm{s,N}}}} \Delta_{\mathrm{L},2}$ to R_0.

Finally, we derive the mean interference from the gNBs. Because of the lack of knowledge of the PGFL of MHCPP, we assume gNBs as a virtual PPP with a density of λ_{m} to approximate the mean interference, which has been verified to provide a good approximation in [31]. Consequently, with the help of the PGFL of PPP, we have (34), as shown at the top of the next page, where $\hat{\sigma}_{\mathrm{m}} = 0.1\zeta_{\mathrm{m}} \ln 10$. The solution for $\mathbb{P}\left(\mathrm{SINR}_{\mathbf{0}\mathbf{x}_{\mathrm{s}}^{\mathrm{N}}} > \tau\right)$ can be similarly derived.

B. SOLUTION OF $\mathbb{P}\left(SINR_{\hat{\mathbf{0}}\mathbf{x}_{\mathrm{m}}} > \tau\right)$

Likewise, the SINR coverage for the typical backhaul link $\mathbb{P}\left(\mathrm{SINR}_{\hat{\mathbf{0}}\mathbf{x}_{\mathrm{m}}} > \tau\right)$ can be approximated in a manner similar to (32). The mean interference from LoS/NLoS IAB-nodes can be derived from a similar step in (33) with an integration limit from 0 to R_0 because the typical IAB-node can only be served by the gNB.

As for the mean interference from other gNBs, we still use the PGFL of PPP to make the approximation, which is given in (35), as shown at the top of the next page, where $\mathcal{G}_{\mathrm{b}} = \frac{\tau K N_{\mathrm{m}}^2 \left(1+\frac{1}{1.5\cdot 2^{2q}}\right)}{P_{\mathrm{m}} N_{\mathrm{T}}^{\mathrm{m}} (N_{\mathrm{R}}^{\mathrm{s}})^2 \left(1-\frac{\tau}{1.5\cdot 2^{2q}}\right)}$, $\mathcal{G}_{\mathrm{b},t} = \mathcal{G}_{\mathrm{b}} M_{\mathrm{m}} e^{-(\sqrt{2}\hat{\sigma}_{\mathrm{m}}\nu_t + \hat{\mu})}$, $r_{\mathrm{b}} = \sqrt{r^2 + r_0^2 - 2rr_0\cos(\vartheta)}$, $\rho_{\mathrm{M}}(r_0)$ is the thinning probability derived in [23, Lemma 1].

C. SOLUTION OF $\mathbb{P}\left(SINR_{\mathbf{0}\mathbf{x}_{\mathrm{m}}} > \tau\right)$

Similarly, the SINR coverage for the gNB-associated access $\mathbb{P}\left(\mathrm{SINR}_{\mathbf{0}\mathbf{x}_{\mathrm{m}}} > \tau\right)$ can be approximated by following the steps in (32). The mean interference from LoS/NLoS IAB-nodes follows the similar way as in (33), with the integration limit from $r_{\mathrm{m}}^{\frac{\alpha_{\mathrm{m}}}{\alpha_{\mathrm{s},j}}} \Delta_j$ to R_0, where $j \in \{\mathrm{L}, \mathrm{N}\}$. The mean interference from other gNBs can be approximated in a manner similar to that in (35).

APPENDIX E
SOLUTION OF THEOREM 3

According to [24, Lemma 2], we have

$$\bar{\mathbb{R}}_{\mathrm{m}} = \mathbb{E}\{W \log_2(1+\mathrm{SINR}_{\mathbf{0}\mathbf{x}_{\mathrm{m}}})\} = \left(1-\frac{1}{N_{\mathrm{T}}^{\mathrm{m}}}\right)^{N_{\mathrm{m}}-1} \times \int_0^{R_0} \frac{W}{\ln 2} \int_0^{\infty} \mathbb{E}\left\{ e^{-z\left(\frac{I_{\mathrm{m,a}}+I_{\mathrm{s,a}}^{\mathrm{L}}+I_{\mathrm{s,a}}^{\mathrm{N}}}{\sigma_{\mathrm{n}}^2 N_{\mathrm{R}}^{\mathrm{u}}} + \frac{\frac{1}{1.5\cdot 2^{2q}} G_{\mathrm{a,m}}}{\left(1+\frac{1}{1.5\cdot 2^{2q}}\right)\sigma_{\mathrm{n}}^2 N_{\mathrm{R}}^{\mathrm{u}}}\right)} \right\}$$

$$\mathbb{E}\left\{ e^{-\mathcal{G}_{\mathrm{s},t} r_{\mathrm{s,L}}^{\alpha_{\mathrm{s,L}}} \hat{I}_{\mathrm{s,a}}^{\mathrm{L}}} \right\} \overset{(c)}{\approx} \mathbb{E}\left\{ \prod_{r_{\mathrm{a,L}} > r_{\mathrm{s,L}}} \frac{1}{\sum_{p=1}^{T} w_p} \sum_{p=1}^{T} \frac{w_p M_{\mathrm{s,L}}^{M_{\mathrm{s,L}}} e^{-M_{\mathrm{s,L}}(\sqrt{2}\hat{\sigma}_{\mathrm{s,L}}\nu_p + \hat{\mu})}}{\left(\mathcal{G}_{\mathrm{s},t} \frac{P_{\mathrm{s}} N_{\mathrm{T}}^{\mathrm{s}} (N_{\mathrm{R}}^{\mathrm{u}})^2 r_{\mathrm{s,L}}^{\alpha_{\mathrm{s,L}}}}{K N_{\mathrm{s}} r_{\mathrm{a,L}}^{\alpha_{\mathrm{s,L}}}} p_{\mathrm{BF}}(N_{\mathrm{T}}^{\mathrm{s}}, N_{\mathrm{R}}^{\mathrm{u}}, N_{\mathrm{s}}) + M_{\mathrm{s,L}} e^{-(\sqrt{2}\hat{\sigma}_{\mathrm{s,L}}\nu_p + \hat{\mu})}\right)^{M_{\mathrm{s,L}}}} \right\}$$

$$\overset{(d)}{=} e^{-2\pi \int_{r_{\mathrm{s,L}}}^{R_0} \lambda_{\mathrm{s,L}}(r_{\mathrm{a,L}}) r_{\mathrm{a,L}} \left[1 - \frac{1}{\sum_{p=1}^{T} w_p} \sum_{p=1}^{T} \frac{w_p M_{\mathrm{s,L}}^{M_{\mathrm{s,L}}} e^{-M_{\mathrm{s,L}}(\sqrt{2}\hat{\sigma}_{\mathrm{s,L}}\nu_p + \hat{\mu})}}{\left(\mathcal{G}_{\mathrm{s},t} \frac{P_{\mathrm{s}} N_{\mathrm{T}}^{\mathrm{s}} (N_{\mathrm{R}}^{\mathrm{u}})^2 r_{\mathrm{s,L}}^{\alpha_{\mathrm{s,L}}}}{K N_{\mathrm{s}} r_{\mathrm{a,L}}^{\alpha_{\mathrm{s,L}}}} p_{\mathrm{BF}}(N_{\mathrm{T}}^{\mathrm{s}}, N_{\mathrm{R}}^{\mathrm{u}}, N_{\mathrm{s}}) + M_{\mathrm{s,L}} e^{-(\sqrt{2}\hat{\sigma}_{\mathrm{s,L}}\nu_p + \hat{\mu})}\right)^{M_{\mathrm{s,L}}}} \right] \mathrm{d}r_{\mathrm{a,L}}}$$

$$\overset{(e)}{=} \prod_{i \in p_{\mathrm{BF}}(N_{\mathrm{T}}^{\mathrm{s}}, N_{\mathrm{R}}^{\mathrm{u}}, N_{\mathrm{s}})} e^{-2\pi \int_{r_{\mathrm{s,L}}}^{R_0} \lambda_{\mathrm{s,L}}(r_{\mathrm{a,L}}) r_{\mathrm{a,L}} \left[1 - \frac{1}{\sum_{p=1}^{T} w_p} \sum_{p=1}^{T} \frac{w_p M_{\mathrm{s,L}}^{M_{\mathrm{s,L}}} e^{-M_{\mathrm{s,L}}(\sqrt{2}\hat{\sigma}_{\mathrm{s,L}}\nu_p + \hat{\mu})}}{\left(\mathcal{G}_{\mathrm{s},t} \frac{P_{\mathrm{s}} N_{\mathrm{T}}^{\mathrm{s}} (N_{\mathrm{R}}^{\mathrm{u}})^2 r_{\mathrm{s,L}}^{\alpha_{\mathrm{s,L}}}}{K N_{\mathrm{s}} r_{\mathrm{a,L}}^{\alpha_{\mathrm{s,L}}}} b_i + M_{\mathrm{s,L}} e^{-(\sqrt{2}\hat{\sigma}_{\mathrm{s,L}}\nu_p + \hat{\mu})}\right)^{M_{\mathrm{s,L}}}} \right] c_i \mathrm{d}r_{\mathrm{a,L}}}, \tag{33}$$

$$\mathbb{E}\left\{e^{-\mathcal{G}_{\mathrm{s},t} r_{\mathrm{s,L}}^{\alpha_{\mathrm{s,L}}} \hat{I}_{\mathrm{m,a}}}\right\} \approx \prod_{\substack{i\in \\ p_{\mathrm{BF}}(N_{\mathrm{T}}^{\mathrm{m}},N_{\mathrm{R}}^{\mathrm{u}},N_{\mathrm{m}})}} e^{-2\pi \int_{r_{\mathrm{s,L}}^{\alpha_{\mathrm{s,L}}/\alpha_{\mathrm{m}}}}^{R_0} \lambda_{\mathrm{m}} \left[1-\frac{1}{\sum_{p=1}^{T} w_p} \sum_{p=1}^{T} \frac{w_p M_{\mathrm{m}}^{M_{\mathrm{m}}} e^{-M_{\mathrm{m}}(\sqrt{2}\hat{\sigma}_{\mathrm{m}} \nu_p+\hat{\mu})}}{\left(\mathcal{G}_{\mathrm{s},t} \frac{P_{\mathrm{m}} N_{\mathrm{T}}^{\mathrm{m}} (N_{\mathrm{R}}^{\mathrm{u}})^2 r_{\mathrm{s,L}}^{\alpha_{\mathrm{s,L}}}}{K N_{\mathrm{m}} r_{\mathrm{a}}^{\alpha_{\mathrm{m}}}} b_i + M_{\mathrm{m}} e^{-(\sqrt{2}\hat{\sigma}_{\mathrm{m}} \nu_p+\hat{\mu})}\right)^{M_{\mathrm{m}}}}\right] c_i r_{\mathrm{a}} \mathrm{d}r_{\mathrm{a}} \Delta_{\mathrm{L},1}}, \quad (34)$$

$$\mathbb{E}\left\{e^{-\mathcal{G}_{\mathrm{b},t} r^{\alpha_{\mathrm{m}}} I_{\mathrm{m,b}}}\right\} \approx \prod_{\substack{i\in \\ p_{\mathrm{BF}}(N_{\mathrm{T}}^{\mathrm{m}},N_{\mathrm{R}}^{\mathrm{s}},N_{\mathrm{m}})}} e^{-\int_0^{2\pi} \int_{\xi}^{R_0} \widetilde{\lambda}_{\mathrm{m}} \rho_{\mathrm{M}}(r_0) \left[1-\frac{1}{\sum_{p=1}^{T} w_p} \sum_{p=1}^{T} \frac{w_p M_{\mathrm{m}}^{M_{\mathrm{m}}} e^{-M_{\mathrm{m}}(\sqrt{2}\hat{\sigma}_{\mathrm{m}} \nu_p+\hat{\mu})}}{\left(\mathcal{G}_{\mathrm{b},t} \frac{P_{\mathrm{m}} N_{\mathrm{T}}^{\mathrm{m}} (N_{\mathrm{R}}^{\mathrm{s}})^2 r^{\alpha_{\mathrm{m}}}}{K N_{\mathrm{m}} r_{\mathrm{b}}^{\alpha_{\mathrm{m}}}} b_i + M_{\mathrm{m}} e^{-(\sqrt{2}\hat{\sigma}_{\mathrm{m}} \nu_p+\hat{\mu})}\right)^{M_{\mathrm{m}}}}\right] c_i r_0 \mathrm{d}r_0 \mathrm{d}\vartheta}, \quad (35)$$

$$\times \left(1-\mathbb{E}\left\{e^{-z \frac{G_{\mathrm{a,m}}}{\left(1+\frac{1}{1.5\cdot 2^{2q}}\right)\sigma_{\mathrm{n}}^2 N_{\mathrm{R}}^{\mathrm{u}}}}\right\}\right) \frac{e^{-z}}{z} \mathrm{d}z \hat{f}_{R_{\mathbf{x}_{\mathrm{m}}\mathbf{0}}}(r) \mathrm{d}r. \quad (36)$$

Similar to the process in Appendix-D, we can obtain the solution by leveraging the approximated Laplace transform of the composite GL distribution in (29) and the PGFL of PPP. Similarly, $\bar{\mathbb{R}}_{\mathrm{s,L}}$, $\bar{\mathbb{R}}_{\mathrm{s,N}}$ and $\bar{\mathbb{R}}_{\mathrm{b}}$ can be derived easily.

ACKNOWLEDGMENT

This work is based on the Ph.D. dissertation [1] of Junkai Zhang. Junkai Zhang was with the Institute for Imaging, Data and Communications, The University of Edinburgh, Edinburgh, U.K, and he is now working with the School of Mathematics and Statistics, Xi'an Jiaotong University, Xi'an, China.

REFERENCES

[1] J. Zhang, "In-band-full-duplex integrated access and backhaul enabled next generation wireless networks," Ph.D. dissertation, Dept. Inst. Imaging, Data, Commun., Univ. Edinburgh, Edinburgh, U.K., Jun. 2023. [Online]. Available: https://era.ed.ac.uk/handle/1842/41226

[2] J. Zhang, N. Garg, M. Holm, and T. Ratnarajah, "Design of full duplex millimeter-wave integrated access and backhaul networks," *IEEE Wireless Commun.*, vol. 28, no. 1, pp. 60–67, Feb. 2021.

[3] T. Zhang, S. Biswas, and T. Ratnarajah, "An analysis on wireless edge caching in in-band full-duplex FR2-IAB networks," *IEEE Access*, vol. 8, pp. 164987–165002, 2020.

[4] S. Park, A. Alkhateeb, and R. W. Heath, "Dynamic subarrays for hybrid precoding in wideband mmWave MIMO systems," *IEEE Trans. Wireless Commun.*, vol. 16, no. 5, pp. 2907–2920, May 2017.

[5] M. N. Kulkarni, A. Ghosh, and J. G. Andrews, "A comparison of MIMO techniques in downlink millimeter wave cellular networks with hybrid beamforming," *IEEE Trans. Commun.*, vol. 64, no. 5, pp. 1952–1967, May 2016.

[6] Z. Xiao, P. Xia, and X.-G. Xia, "Full-duplex millimeter-wave communication," *IEEE Wireless Commun.*, vol. 24, no. 6, pp. 136–143, Dec. 2017.

[7] A. C. Cirik, S. Biswas, S. Vuppala, and T. Ratnarajah, "Beamforming design for full-duplex MIMO interference channels–QoS and energy-efficiency considerations," *IEEE Trans. Commun.*, vol. 64, no. 11, pp. 4635–4651, Nov. 2016.

[8] H. Luo, A. Bishnu, and T. Ratnarajah, "Design and analysis of in-band full-duplex private 5G networks using FR2 band," *IEEE Access*, vol. 9, pp. 166886–166905, 2021.

[9] A. Bishnu, M. Holm, and T. Ratnarajah, "Performance evaluation of full-duplex IAB multi-cell and multi-user network for FR2 band," *IEEE Access*, vol. 9, pp. 72269–72283, 2021.

[10] J. Zhang, H. Luo, N. Garg, M. Holm, and T. Ratnarajah, "Design and analysis of mmWave full-duplex integrated access and backhaul networks," in *Proc. IEEE ICC*, Jun. 2021, pp. 1–6.

[11] J. Zhang, H. Luo, N. Garg, A. Bishnu, M. Holm, and T. Ratnarajah, "Design and analysis of wideband in-band-full-duplex FR2-IAB networks," *IEEE Trans. Wireless Commun.*, vol. 21, no. 6, pp. 4183–4196, Jun. 2022.

[12] 3GPP, *NR; Study on Integrated Access and Backhaul*, document TR 38.874, Rel. 16, Dec. 2018.

[13] J. García-Rois, R. Banirazi, F. J. González-Castaño, B. Lorenzo, and J. C. Burguillo, "Delay-aware optimization framework for proportional flow delay differentiation in millimeter-wave backhaul cellular networks," *IEEE Trans. Commun.*, vol. 66, no. 5, pp. 2037–2051, May 2018.

[14] C. Saha, M. Afshang, and H. S. Dhillon, "Bandwidth partitioning and downlink analysis in millimeter wave integrated access and backhaul for 5G," *IEEE Trans. Wireless Commun.*, vol. 17, no. 12, pp. 8195–8210, Dec. 2018.

[15] M. Polese, M. Giordani, T. Zugno, A. Roy, S. Goyal, D. Castor, and M. Zorzi, "Integrated access and backhaul in 5G mmWave networks: Potential and challenges," *IEEE Commun. Mag.*, vol. 58, no. 3, pp. 62–68, Mar. 2020.

[16] C. Saha and H. S. Dhillon, "Millimeter wave integrated access and backhaul in 5G: Performance analysis and design insights," *IEEE J. Sel. Areas Commun.*, vol. 37, no. 12, pp. 2669–2684, Dec. 2019.

[17] S. Singh, M. N. Kulkarni, A. Ghosh, and J. G. Andrews, "Tractable model for rate in self-backhauled millimeter wave cellular networks," *IEEE J. Sel. Areas Commun.*, vol. 33, no. 10, pp. 2196–2211, Oct. 2015.

[18] T. S. Rappaport, S. Sun, R. Mayzus, H. Zhao, Y. Azar, K. Wang, G. N. Wong, J. K. Schulz, M. Samimi, and F. Gutierrez, "Millimeter wave mobile communications for 5G cellular: It will work!" *IEEE Access*, vol. 1, pp. 335–349, 2013.

[19] T. Bai and R. W. Heath, "Coverage and rate analysis for millimeter-wave cellular networks," *IEEE Trans. Wireless Commun.*, vol. 14, no. 2, pp. 1100–1114, Feb. 2015.

[20] H.-S. Jo, Y. J. Sang, P. Xia, and J. G. Andrews, "Heterogeneous cellular networks with flexible cell association: A comprehensive downlink SINR analysis," *IEEE Trans. Wireless Commun.*, vol. 11, no. 10, pp. 3484–3495, Oct. 2012.

[21] Y. Zhu, G. Zheng, and M. Fitch, "Secrecy rate analysis of UAV-enabled mmWave networks using Matérn hardcore point processes," *IEEE J. Sel. Areas Commun.*, vol. 36, no. 7, pp. 1397–1409, Jul. 2018.

[22] S. S. Kalamkar and M. Haenggi, "Simple approximations of the SIR meta distribution in general cellular networks," *IEEE Trans. Commun.*, vol. 67, no. 6, pp. 4393–4406, Jun. 2019.

[23] J. Lyu and H.-M. Wang, "Secure UAV random networks with minimum safety distance," *IEEE Trans. Veh. Technol.*, vol. 70, no. 3, pp. 2856–2861, Mar. 2021.

[24] H. He, S. Biswas, P. Aquilina, T. Ratnarajah, and J. Yang, "Performance analysis of multi-cell full-duplex cellular networks," *IEEE Access*, vol. 8, pp. 206914–206930, 2020.
[25] H. He, J. Xue, T. Ratnarajah, F. A. Khan, and C. B. Papadias, "Modeling and analysis of cloud radio access networks using Matérn hard-core point processes," *IEEE Trans. Wireless Commun.*, vol. 15, no. 6, pp. 4074–4087, Jun. 2016.
[26] A. Sharma, R. K. Ganti, and J. K. Milleth, "Joint backhaul-access analysis of full duplex self-backhauling heterogeneous networks," *IEEE Trans. Wireless Commun.*, vol. 16, no. 3, pp. 1727–1740, Mar. 2017.
[27] A. Thornburg, T. Bai, and R. W. Heath, "Performance analysis of outdoor mmWave ad hoc networks," *IEEE Trans. Signal Process.*, vol. 64, no. 15, pp. 4065–4079, Aug. 2016.
[28] M. N. Kulkarni, A. Alkhateeb, and J. G. Andrews, "A tractable model for per user rate in multiuser millimeter wave cellular networks," in *Proc. 49th Asilomar Conf. Signals, Syst. Comput.*, Nov. 2015, pp. 328–332.
[29] K. Cho, J. Lee, and C. G. Kang, "Stochastic geometry-based coverage and rate analysis under Nakagami & log-normal composite fading channel for downlink cellular networks," *IEEE Commun. Lett.*, vol. 21, no. 6, pp. 1437–1440, Jun. 2017.
[30] M. Haenggi, *Stochastic Geometry for Wireless Networks*. Cambridge, U.K.: Cambridge Univ. Press, 2012.
[31] M. Haenggi, "Mean interference in hard-core wireless networks," *IEEE Commun. Lett.*, vol. 15, no. 8, pp. 792–794, Aug. 2011.
[32] T. Bai, R. Vaze, and R. W. Heath, "Analysis of blockage effects on urban cellular networks," *IEEE Trans. Wireless Commun.*, vol. 13, no. 9, pp. 5070–5083, Sep. 2014.
[33] M. Nakagami, "The *m*-distribution—A general formula of intensity distribution of rapid fading," in *Statistical Methods in RadioWave Propagation*. Oxford, U.K.: Pergamon, 1960.
[34] C. Zhong, M. Matthaiou, G. K. Karagiannidis, and T. Ratnarajah, "Generic ergodic capacity bounds for fixed-gain AF dual-hop relaying systems," *IEEE Trans. Veh. Technol.*, vol. 60, no. 8, pp. 3814–3824, Oct. 2011.
[35] A. M. Sayeed, "Deconstructing multiantenna fading channels," *IEEE Trans. Signal Process.*, vol. 50, no. 10, pp. 2563–2579, Oct. 2002.
[36] O. E. Ayach, R. W. Heath, S. Abu-Surra, S. Rajagopal, and Z. Pi, "The capacity optimality of beam steering in large millimeter wave MIMO systems," in *Proc. IEEE SPAWC*, Jun. 2012, pp. 100–104.
[37] C. Balanis, *Antenna Theory*. Hoboken, NJ, USA: Wiley, 1997.
[38] I. P. Roberts, J. G. Andrews, and S. Vishwanath, "Hybrid beamforming for millimeter wave full-duplex under limited receive dynamic range," *IEEE Trans. Wireless Commun.*, vol. 20, no. 12, pp. 7758–7772, Dec. 2021.
[39] R. Giuliano and F. Mazzenga, "Exponential effective SINR approximations for OFDM/OFDMA-based cellular system planning," *IEEE Trans. Wireless Commun.*, vol. 8, no. 9, pp. 4434–4439, Sep. 2009.
[40] A. Oborina, M. Moisio, and V. Koivunen, "Performance of mobile MIMO OFDM systems with application to UTRAN LTE downlink," *IEEE Trans. Wireless Commun.*, vol. 11, no. 8, pp. 2696–2706, Aug. 2012.
[41] S. Singh, H. S. Dhillon, and J. G. Andrews, "Offloading in heterogeneous networks: Modeling, analysis, and design insights," *IEEE Trans. Wireless Commun.*, vol. 12, no. 5, pp. 2484–2497, May 2013.
[42] A. Al-Hourani, R. J. Evans, and S. Kandeepan, "Nearest neighbor distance distribution in hard-core point processes," *IEEE Commun. Lett.*, vol. 20, no. 9, pp. 1872–1875, Sep. 2016.
[43] C. Chen, R. C. Elliott, and W. A. Krzymien, "Empirical distribution of nearest-transmitter distance in wireless networks modeled by Matérn hard core point processes," *IEEE Trans. Veh. Technol.*, vol. 67, no. 2, pp. 1740–1749, Feb. 2018.
[44] *IEEE Standard for Information Technology—Telecommunications and Information Exchange Between Systems—Local and Metropolitan Area Networks—Specific Requirements—Part 11: Wireless LAN Medium Access Control (MAC) and Physical Layer (PHY) Specifications Amendment 3: Enhancements for Very High Throughput in the 60 GHz Band*, Standard 802.11ad-2012, pp. 1–628, Dec. 2012.
[45] A. I. Sulyman, A. T. Nassar, M. K. Samimi, G. R. Maccartney, T. S. Rappaport, and A. Alsanie, "Radio propagation path loss models for 5G cellular networks in the 28 GHZ and 38 GHZ millimeter-wave bands," *IEEE Commun. Mag.*, vol. 52, no. 9, pp. 78–86, Sep. 2014.
[46] J. Zhang, L. Dai, X. Li, Y. Liu, and L. Hanzo, "On low-resolution ADCs in practical 5G millimeter-wave massive MIMO systems," *IEEE Commun. Mag.*, vol. 56, no. 7, pp. 205–211, Jul. 2018.
[47] I. Glover and P. M. Grant, *Digital Communications*. London, U.K.: Pearson Education, 2010.
[48] S. Ahmed, T. Ratnarajah, M. Sellathurai, and C. Cowan, "Iterative receivers for MIMO-OFDM and their convergence behavior," *IEEE Trans. Veh. Technol.*, vol. 58, no. 1, pp. 461–468, Jan. 2009.
[49] H. E. Salzer, R. Zucker, and R. Capuano, "Table of the zeros and weight factors of the first 20 Hermite polynomials," *J. Res. Nat. Bur. Standards*, vol. 48, no. 2, p. 111, Feb. 1952.
[50] F. Olver, D. Lozier, R. Boisvert, and C. Clark, *NIST Handbook of Mathematical Functions*. Cambridge, U.K.: Cambridge Univ. Press, 2010.

JUNKAI ZHANG (Member, IEEE) received the B.Eng. degree in communication engineering from Shenyang Ligong University, China, in 2018, the M.Sc. degree (Hons.) in signal processing and communications from The University of Edinburgh, U.K., in 2019, and the Ph.D. degree in engineering (wireless communications) from the Institute for Imaging, Data and Communications, The University of Edinburgh, in 2023. He is currently with the School of Mathematics and Statistics, Xi'an Jiaotong University, Xi'an, China, as a Research Assistant. His research interests include 6G AI-based wireless communications, millimeter-wave communications, in-band-full-duplex radio, stochastic geometry, and integrated sensing and communications.

THARMALINGAM RATNARAJAH (Senior Member, IEEE) is currently with the Institute for Imaging, Data and Communications, The University of Edinburgh, U.K., as a Professor of digital communications and signal processing. He was the Lead Coordinator of European Union (EU) Project HARP (4.6M) in the area of highly distributed MIMO and ADEL (3.7M) in the area of licensed shared access. He was the Coordinator of European Union Future and Emerging Technologies Project CROWN (3.4M) in the area of cognitive radio networks and HIATUS (3.6M) in the area of interference alignment. His research interests include signal processing and information-theoretic aspects of beyond 5G cellular networks, full-duplex radio, mmWave communications, random matrix theory, big data analytics and machine learning for wireless networks, statistical and array signal processing, and physical-layer secrecy and interference alignment. He has published over 450 peer-reviewed articles in these areas and holds four U.S. patents. He is a fellow of the Higher Education Academy (FHEA). He was an Associate Editor of IEEE TRANSACTIONS ON SIGNAL PROCESSING 2015–2017 and the Technical Co-Chair of the 17th IEEE International Workshop on Signal Processing Advances in Wireless Communications, Edinburgh, U.K., in July 2016.